IEEE Open Journal of the
Industrial Electronics Society

Received 21 May 2024; accepted 23 June 2024. Date of publication 4 July 2024;
date of current version 18 July 2024. The review of this article was arranged by Associate Editor H. M. Suryawanshi.

Digital Object Identifier 10.1109/OJIES.2024.3421669

Hierarchical Fuzzy Framework for EV Supported Islanded Microgrid Frequency Stabilization

ABDUL LATIF[1] (Member, IEEE), S. M. SUHAIL HUSSAIN[2,3] (Senior Member, IEEE), AHMED AL-DURRA[1] (Senior Member, IEEE), AND ATIF IQBAL[4] (Fellow, IEEE)

[1]Advanced Power and Energy Center, EECS Department, Khalifa University, Abu Dhabi 127788, UAE
[2]Electrical Engineering Department, King Fahd University of Petroleum and Minerals, Dhahran 31261, Saudi Arabia
[3]Interdisciplinary Research Center for Sustainable Energy Systems, King Fahd University of Petroleum and Minerals, Dhahran 31261, Saudi Arabia
[4]Electrical Engineering Department, Qatar University, Doha 2713, Qatar

CORRESPONDING AUTHOR: ATIF IQBAL (e-mail: atif.iqbal@qu.edu.qa)

This work was supported in part by the NPRP under Grant 13S-0108-200028 from the Qatar National Research Fund (a member of Qatar Foundation), and in part by the Qatar National Library, Doha, Qatar.

ABSTRACT This article delves into the intricate challenge of frequency stabilization within islanded microgrids (IMGs), particularly exacerbated by the integration of low-inertia renewable power generations. A hierarchical control strategy is proposed, comprising a fuzzy rule-based controller, a two-degree-of-freedom fractional-order PI controller, and a proportional resonant controller. The bolstering of frequency stabilization is achieved by the integration of aggregated electric vehicle storage into the IMG. Adaptive tuning of the fuzzy rule-based load frequency controller's parameters is facilitated by a novel quasi-oppositional prairie dog technique (QOPDT), developed within this study. A comprehensive comparison is conducted between the efficacy of the QOPDT technique and various other optimization methods. Significant improvements in system frequency stability across diverse scenarios are observed with the adoption of the QOPDT-based controller, as evidenced by qualitative assessment. Furthermore, the investigation extends to consider the impact of time-varying delay on the integrated electric vehicle system, broadening the scope of the investigation. Validation of the effectiveness and practicality of the proposed control framework is undertaken utilizing the real-time OPAL-RT 5700 testbed platform.

INDEX TERMS Electric vehicle (EV), fuzzy rule-based control (FRC), load frequency regulation (LFR), quasi-oppositional prairie dog technique (QOPDT), communication delay.

I. INTRODUCTION

The rising demand for electrical supply has led to an increase in power generation from renewable energy sources, culminating in the integration of renewable power generation (RPG) with backup generators and storage systems. Renewable energy sources are increasingly integrated into power generation, driven by the depletion of conventional fossil fuel reserves at an alarming rate. Unlike fossil fuels, which take hundreds of years to form within the Earth's crust, renewable sources such as wind, solar, solar-thermal, and tidal energy offer sustainable alternatives. However, these sources, including the sun and wind, exhibit erratic behavior, unable to consistently supply electricity throughout the day [1]. At the same time, the emergence of heavy-duty industries has further escalated the demand for power, leading to decentralized microgrid power systems. Islanded microgrid (IMG) systems have emerged as effective configurations for efficiently managing generation and distribution while minimizing losses [2]. Nevertheless, the growing penetration of RPGs into these power grids has posed significant challenges, as the imbalance between load and generation results in high instability and low inertia. This imbalance results in frequency fluctuations within the microgrid [2]. Such fluctuations are problematic because they not only impact the stability of the grid, but also affect the power distribution. Additionally, unstable frequencies can potentially damage end-user equipment. To address

this issue, frequency regulation on the demand side, termed load frequency stabilization, becomes crucial [3]. This model aims to balance the load frequency and mitigate unscheduled power interchange between generators. The primary goal of load frequency control is to maintain the frequency of the load within a constant and tolerable limit by achieving a zero steady-state error [4]. Despite the advantages of renewable energy sources, such as their eco-friendliness and sustainability, the integration of solely renewable and hybridized RPG-cogeneration presents a significant challenge: how to maintain stable frequencies in the face of fluctuating renewable energy inputs and varying load demands [5]. This constitutes the problem statement of the current study.

Research into load frequency regulation (LFR) in microgrids has gained urgency due to several factors. Integration of renewable energy sources, such as solar and wind, introduces issues such as higher voltage spikes in the distribution and frequency imbalances. Traditional frequency control methods, usually governed by the speed of distributed energy generators, are often insufficient to handle these fluctuations and load instabilities. Researchers have explored various control methods to address this problem, ranging from traditional controller-based LFR [6], [7] to more advanced model-based strategies, such as sliding mode controller and model predictive controller [8], [9]. However, these approaches often fall short when operating points vary significantly, leading to a surge in interest in model-free controllers, specifically fuzzy rule-based control (FRC) [10], [11] and fractional order control (FOC) [12], [13]. FRC has been widely used in the electric power sector, offering improved performance in situations that include uncertain nonlinear loads and signal perturbations [14]. FOC, on the other hand, provides more degrees of freedom for controller parameter design, enabling greater adaptability and robust dynamic performance. A combination of these, termed fuzzy rule-based fractional-order control (FR-FOC), has been presented in past studies [15], [16], [17], [18], [19]. This controller adjusts its control parameters based on the operating point and has been applied in isolated microgrids to showcase its robustness with reduced computational load. Despite its advantages, it has limitations in monitoring set points and effectively reducing external distortions [18]. Given the shortcomings of existing solutions, the focus is shifting toward controllers with higher disturbance rejection capacity and faster convergence rates. Two degree-of-freedom (TDOF) controllers satisfy these needs. Fuzzy rule-based TDOF controllers have shown promise in various applications, including permanent magnet synchronous linear motors [20] and power system stability [21], [22]. Therefore, the current study aims to develop a modified fuzzy rule-based TDOF controller to address these challenges more effectively. This controller is designed to adaptively handle current issues without compromising the overall efficiency of the system. Therefore, the problem statement for this study focuses on developing an adaptive, efficient, and robust TDOF controller for LFR in microgrids with integrated renewable energy sources.

Building on the established need for an adaptive, efficient, and robust TDOF controller for LFR in microgrids, it becomes vital to also focus on the optimization techniques used for setting the controller's coefficients. Previous research has explored various optimization algorithms, including particle swarm optimization [23], the ICA technique [6], the modified blackhole optimization algorithm [18], and others such as quasi-oppositional Harris hawk optimization [24] and supply demand optimization [25]. The No-Free-Lunch (NFL) theorem asserts that no single algorithm can effectively solve every optimization problem. This realization opens up continuous possibilities for enhancing the performance of solutions by employing advanced meta-heuristic techniques, which are particularly aimed at optimizing the balance between the exploration and exploitation stages of problem-solving [26]. In a notable advancement, Ezugwu et al. [27] have introduced a novel, robust swarm-based optimization strategy termed the prairie dog technique (PDT). This method, inspired by the foraging patterns of prairie dog, is designed to address a broad spectrum of optimization challenges. The PDT is characterized by its simplicity, flexibility, and a derivation-free approach, attributes that together provide substantial benefits in its practical application. However, it is observed that PDT gets trapped in more frequent local optima and there is less population diversity when compared with other optimization techniques. Therefore, there exists a research gap to effectively compare and improve optimization techniques such as PDT to solve LFR problems in power systems. The current study aims to fill this gap by employing a quasi-oppositional-based learning approach (QOBL) [28] to the original PDT, creating a modified version called quasi-oppositional PDT (QOPDT). This improves the convergence rate, making it a powerful tool for solving the LFR problem. Table 1 provides a detailed comparison of this study to the existing body of literature on the topic.

Specifically, the contributions of this article are fourfold.

- The transient characteristics of the test microgrid network's hierarchical frequency-control scheme are investigated, considering the intermittent nature wind interactive doubly-fed induction generator (DFIG) based wind turbines (WTs), the inherent governor reference control nonlinearity of Coordinated Synchronous MicroTurbine (CSμT), and electric vehicles (EVs).
- A novel fuzzy rule-based TDOF fractional tilt-integral with proportional resonant (FR-TDOF-FTI-(PR)) controller is designed, and a comparative dynamic response analysis is conducted.
- The QOPDT is developed and applied to achieve nearly optimal gains for the proposed controllers, thereby improving the overall performance stability of the system and accelerating the convergence rate of the original PDT.
- An analysis of the impact of an EV aggregator on system stability in the presence of time-varying delays is performed using the QOPDT-tuned controller. This analysis

TABLE 1. Comprehensive Survey of Existing Literature

Ref	*Type of generations*	*Storages*	*Error function (J)*	*Techniques/controller*	*Effect of communication delay*
[2]	Wind, solar PV, diesel	Battery, superconducting magnetic energy storage (SMES), fuel cell (FC)	ISE	TLBO, H2/H∞ controller	X
[6]	PV, wind diesel	Battery	ITAE	ICA, ITDF	X
[7]	Governor-turbine	X	ISE	IMC, PIDD2	√(fixed communication delay)
[8]	Wind, reheat turbine	X	X	FOI-SMC	√(time varying communication delay)
[13]	Wind, PV, conventional reheat thermal, hydro	Capacitive, EV	ITSE	SGO, FOPIDD2	X
[17]	Hydro	EV	X	QPmR, FOPI	√(Fixed communication delay)
[19]	Wind, PV, thermal, Biogas, Geothermal	EV	ITAE	AOAVOA, T2FPD+(2DOF-PID)	√(fixed time delay)
[21]	Wind, PV, Sea Wave	Battery, flywheel	ITSE	MOMBHA, FOFPD+I	√(assume communication delay)
[22]	Generator, exitor	X	ITSE	WCA, 2DOF-PI	X
[24]	Wind, PV, Thermal, Bio-gas,	EV	ITAE	QOHHO, TDOF-LADRC	√(fixed time delay)
This study	Wind, CSμT	EV	ITAE	QOPDT, FR-TDOF-FTI-(PR)	√(time varying communication delay)

incorporates considerations of the stochastic nature of real-time load and RPG.

The organization of this article is as follows. Section II outlines the model for the test system under investigation. Section II also describes the LFR mechanism, focusing on steady-state error and stability evaluations of EVs. Section III presents the recommended controller and the proposed optimization technique, QOPDT. In Section IV, the simulation and experimental performances are examined, and Section V concludes this article.

II. INVESTIGATED MICROGRID'S SYSTEM MODELING

A. CONFIGURATION OF IMG

An IMG system is taken into consideration to drive the LFR strategy. In this section, descriptions of each system component with suitable modeling and a coordinated control strategy are presented for further examination. Such a control method, achieved by designing a novel controller necessitates optimal tuning of its coefficients and gains. These requirements are fulfilled by introducing an innovative optimization technique that includes thorough analyses of both steady-state performance and stability.

The schematic layout of EV-integrated IMG is depicted in Fig. 1, while Fig. 2(a) describes its modeling by displaying information about the brief change in power and frequency. The parameters for the IMG test system are enumerated in Table 2.

B. MODELING OF CSμT SYSTEM

The primary advantage of incorporating the solar tower (ST) solar thermal system within the IMG is its higher efficiency (∼28%). This efficiency is achieved by utilizing a heat transfer

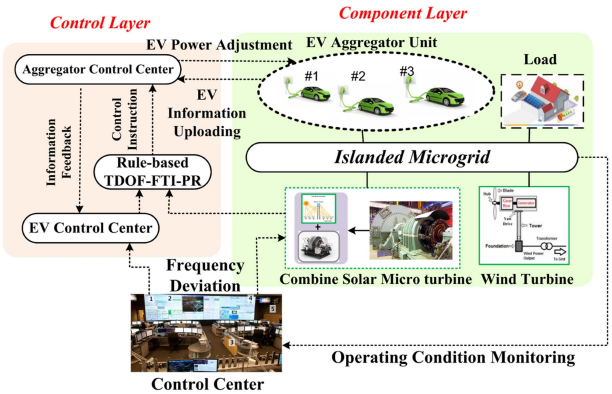

FIGURE 1. Schematic layout of EV participation in LFR of IMG.

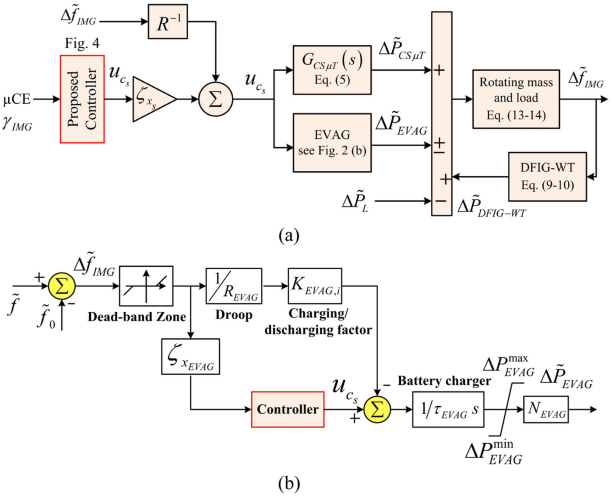

FIGURE 2. (a) Detailed modeling of EV aggregator proposed LFR scheme. (b) Model of EV aggregator for suggested LFR study.

TABLE 2. Parameters of the IMG Test System

Parameters	Values
K_{RFC}, K_{RC}, K_{GV}, K_{TR}	1, 1, 1, 1
T_{RFC}, τ_{RC}, τ_{GV}, τ_{TR}	1.33s, 4s, 0.08s, 1s
K_{VA}, K_{FA}, τ_{VA}, τ_{FA}	1, 1, 0.8 s, 0.3s
$K_{S\mu T}$, $\tau_{S\mu T}$	1, 0.2s
K_{EVAG}, R_{EVAG}	0.0024, 0.045 Hz/p.u
$\Delta P_{EVAG}^{max} = -\Delta P_{EVAG}^{min}$	0.01 p.u.
τ_{EVAG},	0.035 s
$SoC_{EVAG}(0)$	60%
τ_R, τ_w	0.07, 5.8
$K_{WT,P}$, $k_{WT,i}$	2.12, 1.203
GRC	20%
R	2.4 Hz/p.u MW
M	0.166
D	0.015 (p.u/Hz)

stream that employs refrigerant to extract the intense heat necessary to drive the generator, thereby producing electricity. Subsequently, the temperature of the exiting receiver tube can be delineated using the following equation:

$$C.\frac{d}{dt}(T_e) = \alpha R - F_e\left(\frac{T_e - T_{in}}{L}\right) - \gamma\left(\frac{T_e - T_{in}}{2} - T_{ab}\right)$$
$$\text{where; } (T_e - T_{in})/2 = T_{\text{mean}} \; and \; C = \rho cV \tag{1}$$

where C and T_{mean} represent the heat capacity and mean temperature of the receiver fluid, respectively. The definitive state equation for the ST is articulated as follows [29]:

$$\frac{d}{dt}(T_e) = \frac{((\eta_h.A_h.\alpha)/A_{rec})}{C}\varphi_s - \frac{F_e}{LC}(T_e - T_{in}) - \frac{\beta}{C}(T_{\text{mean}} - T_{ab}). \tag{2}$$

By applying linearization to (2), the estimated transfer function for the ST can be represented as follows:

$$G_{ST}(s) = \left(\frac{K_{RFC}}{s\tau_{RFC}+1}\right)\left(\frac{K_{RC}}{s\tau_{RC}+1}\right)\left(\frac{K_{GV}}{s\tau_{GV}+1}\right)\left(\frac{K_{TR}}{s\tau_{TR}+1}\right). \tag{3}$$

Additionally, the use of advanced combustion turbines, combined with higher rotational speeds and lower noise emissions, increases the practicality of the small microturbine (μT) in the integrated microgrid (IMG) system. The linearized transfer function of the μT is described [30] as follows:

$$\left.\begin{aligned} G_{\mu T}(s) &= \left\{\left(\tfrac{K_{VA}}{s\tau_{VA}+1}\right).\left(\tfrac{K_{FA}}{s\tau_{FA}+1}\right).u_{CS\mu T}\right\} \\ \text{where, } u_{CS\mu T} &= \left\{\left(Transfer\,Function\,Controller - R^{-1}\right).\Delta\tilde{f}_{IMG}\right\} \end{aligned}\right\}. \tag{4}$$

Considering the availability of both sources, a unified turbine can be employed to extract power by combining these two generation units. This integration not only boosts efficiency but also facilitates all-day power sharing. The overall transfer function for the proposed CSμT can be articulated as follows:

$$G_{CS\mu T}(s) = \left\{G_{ST}(s) + G_{\mu T}(s).\left(1/s\tau_{S\mu T}+1\right)\right\}. \tag{5}$$

C. MODELING OF DFIG-BASED WIND TURBINE (DFIG-WT)

The modeling of wind power's cooperation with the IMG system for frequency stabilization is elaborated in this section. Inertia problems are typically inherited in a microgrid power system that uses wind integration because of the WT mechanism. When there are load disruptions in the microgrid system, inertia problems cause the system frequency fluctuation and rate of variation of frequency to grow [31]. According to a mathematical proof in [32], the DFIG's controller is able to resolve the inertia problems from wind incorporated IMG system. Therefore, in the current study, a wind energy source paired with the same inertia controller is added to the IMG region to support system frequency. The DFIG controller detects the frequency deviation ($\Delta\tilde{f}_{IMG}$) and supplies an extra power signal $\Delta\tilde{P}$ to the unconventional generator shown in the following:

$$\Delta\tilde{P} = -k_{df}\frac{d.\Delta\tilde{f}0}{dt} - k_{pf}\tilde{f}_0 \tag{6}$$

where k_{df} and k_{pf} are the controller gains linked to the rate of frequency fluctuation and frequency fluctuation, respectively. The inertia and speed controllers are both featured in DFIG. The control channel sends a change in power signals ($\Delta\tilde{P}_w$) to the unconventional generator can be expressed as follows [28]:

$$\Delta\tilde{P}_w = k_{WT,p}\left(\Delta w - \Delta w_{ref}\right) + k_{WT,i}\int\left(\Delta w - \Delta w_{ref}\right).dt \tag{7}$$

where $(\Delta w - \Delta w_{ref})$ input speed difference and $k_{WT,p}$ and $k_{WT,i}$ are gain constants of the speed controller, respectively. The net input power of DFIG is represented in the following:

$$\Delta\tilde{P}_{IN} = \left(\Delta\tilde{P} - \Delta\tilde{P}_w\right). \tag{8}$$

This study considers a true statistical datasheet of the wind power generation station, sourced from NASA [33]. The following equations illustrate the rate of change in DFIG-based WT power at the station under consideration as depicted in the following:

$$\left.\begin{aligned} \tilde{P}_{WT} &= \begin{cases} 0, & w_{WT} < w_{cut-in} \,||\, w_{WT} > w_{cut-out} \\ P_{rated}, & w_{rated} \le w_{WT} \le w_{cut-out} \\ (0.001312\,w_{WT}^6 - 0.04603\,w_{WT}^5 + 0.3314\,w_{WT}^4 \\ +3.687\,w_{WT}^3 - 51.1\,w_{WT}^2 + 2.33\,w_{WT} + 366), & \text{else} \end{cases} \\ \Rightarrow \Delta\tilde{P}_{WT} &= \begin{cases} 0, & w_{WT} < w_{cut-in} \,||\, w_{WT} > w_{cut-out} \\ 0, & w_{rated} \le w_{WT} \le w_{cut-out} \\ ([0.007872\,w_{WT}^5 - 0.23015\,w_{WT}^4 + 1.3256\,w_{WT}^3 \\ +11.061\,w_{WT}^2 - 102.2\,w_{WT} + 2.33].\,\Delta w_{WT}), & \text{else} \end{cases} \end{aligned}\right. \tag{9}$$

where $w_{cut\text{-}in}$ and $w_{cut\text{-}out}$ are the cut-in and cut-out wind speeds.

The overall output power from DFIG ($\Delta\tilde{P}_{DFIG-WT}$) due to Δw_{ref} frequency fluctuation of IMG ($\Delta\tilde{f}_{IMG}$) can be formulated as follows:

$$\Delta\tilde{P}_{DFIG-WT} = -\left(\frac{G_i(s).G_{WT}(s)}{1+G_{sc}(s).G_{WT}(s)}\right).\Delta\tilde{f}_{IMG} - \left(\frac{G_{sc}(s).G_{WT}(s)}{1+G_{sc}(s).G_{WT}(s)}\right).\Delta w_{ref} \quad (10)$$

where;

$$\begin{cases} G_i(s) = \frac{s\tau_w}{(1+s\tau_w).(1+s\tau_R)} \times \left\{-\left(k_{df}+k_{pf}\right)\right\}; \\ G_{sc}(s) = \left(k_{WT,p} + {}^{k_{WT,i}}/_{s}\right);\ G_{WT}(s) = \frac{1}{1+s\tau_A} \end{cases}.$$

D. MODELING OF ELECTRIC VEHICLE AGGREGATOR (EVAG) CONTROL

Fig. 2(b) shows illustrates the EVAG's mathematical model for frequency regulation studies. With the capability to charge and discharge between 5 and 50 kW, EV could be a viable option for the use of noncontracting electricity. EVAG can support LFR service with the desirable state of charge (SoC) of EVAG's battery pack [34]. Here, in Fig. 2(b), the proposed EVAG model consists of a droop-based primary control, a proposed LFR controller, coordinated with a battery charger that manages the power transfer from the battery to the microgrid. The controller action is driven with $\Delta\tilde{f}_{IMG}$, a mismatch between system frequency $\tilde{f}$ and reference $\tilde{f}_0$ frequency. In order to safeguard the device a delay time (δ) is provided by the system. It is clear that the EVAG plays a role in frequency management when the frequency fluctuation transgresses a dead zone of upper and lower boundaries. This stops batteries from being charged or discharged too frequently, preventing battery deterioration. The EV aggregator contributes to LFR service by absorbing power from the system when $\Delta\tilde{f}_{IMG}$ exceeds $\Delta\tilde{f}_{u\_IMG}$ and discharges when goes below $\Delta\tilde{f}_{l\_IMG}$.

The output power from the EVAG based on frequency deviation is as follows (ΔP_{EVAGi}):

$$\Delta\tilde{P}_{EVAG,i} = \begin{cases} K_{EVAG,i}\Delta\tilde{f}_{IMG};\ \left|K_{EVAG,i}\Delta\tilde{f}_{IMG}\right| \le \tilde{P}_{\max} \\ \tilde{P}_{\max};\ K_{EVAG,i}\Delta\tilde{f}_{IMG} > \tilde{P}_{\max} \\ -\tilde{P}_{\max};\ K_{EVAG,i}\Delta\tilde{f}_{IMG} < -\tilde{P}_{\max} \end{cases} \quad (11)$$

$$\Delta\tilde{P}_{EVAG} = N_{EVAG} * \sum_{i=1,2....n} \Delta\tilde{P}_{EVAG,i}. \quad (12)$$

The extracted signal (u_{cs}), issued by the controller, is used to decide whether the $\Delta\tilde{P}_{EVAG}$ will engage in charging or discharging [35]. Where $\tilde{P}_{\max}$ is the maximum power capacity available from a single EVAG, $K_{EVAG,i}$ represents the participation of charging/discharging factors of an individual EVAG. R_{EVAG} and τ_{EVAG} represent the droop factor and time constant of the EVAG.

As depicted in Fig. 2(a), the equation for generation-load balance is as follows:

$$\Delta\tilde{P}_{CS\mu T} + \Delta\tilde{P}_{DFIG-WT} + \Delta\tilde{P}_{EVAG} = \Delta\tilde{P}_L. \quad (13)$$

The variation in frequency deviation (Δf) within the IMG resulting from RRs and load disturbances can be described as follows:

$$\Delta\dot{\tilde{f}}_{IMG} = \left(\frac{1}{\varsigma(s)}\right)\left[\Delta\tilde{P}_{CS\mu T} + \Delta\tilde{P}_{DFIG-WT} \pm \Delta\tilde{P}_{EVAG} - \Delta\tilde{P}_L\right] \quad (14)$$

where $\varsigma(s) = sM+D$ is the denominator. The M and D are the inertia and damping coefficients of rotating mass. $\Delta\tilde{P}_{CS\mu T}$, $\Delta\tilde{P}_{EVAG}$, $\Delta\tilde{P}_{DFIG-WT}$, and $\Delta\tilde{P}_L$ denotes the change in output power of combined solar microturbine, EVAG, DFIG-based WT, and loads, respectively. The change in the combined solar microturbine generator's power can be depicted as follows:

$$\Delta\dot{\tilde{P}}_{CS\mu T} = -\frac{1}{\tau_{S\mu T}}\Delta\tilde{P}_{CS\mu T} + \frac{\tau_{FA}-K_{S\mu T}}{\tau_{FA}.\tau_{S\mu T}}\Delta\tilde{P}_{FA} + \frac{K_{S\mu T}}{\tau_{FA}}\Delta\tilde{P}_{VA} + \frac{\sum K_{i-ST}}{\sum \tau_{i-ST}}\Delta\tilde{P}_{ST}. \quad (15)$$

Similarly, the variation of combustion engine and valve actuator powers ($\Delta\tilde{P}_{FA}$, $\Delta\tilde{P}_{VA}$) can be derived as follows:

$$\left.\begin{aligned} \Delta\dot{\tilde{P}}_{FA} &= -\tfrac{1}{\tau_{FA}}\Delta\tilde{P}_{FA} + \tfrac{1}{\tau_{FA}}\Delta\tilde{P}_{VA} \\ \Delta\dot{\tilde{P}}_{VA} &= -\left(R^{-1}.\tau_{VA}\right)\Delta\tilde{f}_{IMG} - \tfrac{1}{\tau_{VA}}\Delta\tilde{P}_{VA} + \tfrac{1}{\tau_{VA}}u_{CS\mu T} \end{aligned}\right\}. \quad (16)$$

The gains and time values of all the system components are depicted in Table 2 where $u_{CS\mu T}$ denote the control signal of CSμT generation. The participation of "ζ" in Fig. 2 represents the power-sharing coefficients of CSμT and EVAG. The allocation of "ζ" should be $\sum_{x_s}\zeta_{x_s} = 1$.

Where x_s is the subsystems $s \in \{\text{sCS}\mu\text{T}, \text{sEVAG}\}$ associated with "ζ." To be more specific, the input signal (u_{xs}) to corresponding subsystems can be expressed as follows:

$$u_{x_s} = \zeta_{x_s}.u_{c_s} - R^{-1}.\Delta\tilde{f}_{IMG} \quad (17)$$

where u_{cs} is the proposed designed controller's output signal. For more precision, a microgrid control error (μCE) signal with conjugation of biasing factor (β) and $\Delta\tilde{f}_{IMG}$ can be calculated by the following:

$$\gamma_{IMG} = \beta.\Delta\tilde{f}_{IMG} \quad (18)$$

where γ_{IMG} represent the μCE signal. In relation to the change in aggregated EV power in (12), the differential (19) can be used to represent the dynamics of EVAG.

$$\Delta\dot{\tilde{P}}_{EVAG} = -\frac{K_{EVAG}}{R_{EVAG}.\tau_{EVAG}}\Delta\tilde{f}_{IMG} - \frac{1}{\tau_{EVAG}}\Delta\tilde{P}_{EVAG} + \frac{1}{\tau_{EVAG}}u_{EVAG}. \quad (19)$$

The MG test system parameters are listed in Table 2.

Let $x = [\Delta\tilde{f}_{IMG}\ \ \Delta\tilde{P}_{CS\mu T}\ \ \Delta\tilde{P}_{FA}\ \ \Delta\tilde{P}_{VA}\ \ \Delta\tilde{P}_{ST}\ \ \Delta\tilde{P}_{EVAG}]^T$ is the vector of state variables. The plant's disturbance $\Delta\varepsilon = \Delta\tilde{P}_{DFIG-WTG} - \Delta\tilde{P}_L$. Considering the illustrated states of different subsystem, the state space model of the IMG's

test bed can be defined as follows:

$$\begin{cases} \dot{x}(t) = L.x(t) + H.u(t) + F.\Delta\varepsilon(t) \\ \Delta\tilde{f}_{IMG}(t) = J.x(t) \end{cases} \tag{20}$$

where $u = [u_{CS\mu T} \quad u_{EVAG}]^T$ is the control signals' vector. The corresponding matrices and vectors are derived as follows:

$$L = \begin{bmatrix} -\frac{D}{M} & \frac{1}{M} & 0 & 0 & 0 & \frac{1}{M} \\ 0 & \frac{-1}{\tau_{S\mu T}} & \frac{\tau_{FA}-K_{S\mu T}}{\tau_{FA}.\tau_{S\mu T}} & \frac{K_{S\mu T}}{\tau_{FA}} & \frac{\sum K_{i-ST}}{\sum \tau_{i-ST}} & 0 \\ 0 & 0 & \frac{-1}{\tau_{FA}} & \frac{1}{\tau_{FA}} & 0 & 0 \\ -\left(R^{-1}.\tau_{VA}\right) & 0 & 0 & \frac{-1}{\tau_{VA}} & 0 & 0 \\ 0 & 0 & 0 & 0 & -\frac{\sum K_{i-ST}}{\sum \tau_{i-ST}} & 0 \\ \frac{-K_{EVAG}}{R_{EVAG}.\tau_{EVAG}} & 0 & 0 & 0 & 0 & \frac{-1}{\tau_{EVAG}} \end{bmatrix};$$

$$H = \begin{bmatrix} 0 \\ 0 \\ 0 \\ \frac{1}{\tau_{VA}} \\ 0 \\ \frac{1}{\tau_{EVAG}} \end{bmatrix}$$

$$F = \left[\tfrac{1}{M} \quad 0 \quad 0 \quad 0 \quad 0 \quad 0\right]^T; \; J = \left[1 \quad 0 \quad 0 \quad 0 \quad 0 \quad 0\right]. \tag{21}$$

E. STABILITY ANALYSIS AND STEADY STATE ERROR

The coordinating EVAG and CSμT units in LFR service may experience the signals from the central control unit with a considerable time delay. As a result, the system may experience instability causing fluctuation in system frequency. Leveraging time delay in the frequency response loop, the following differential equation can be used to represent the dynamic reaction of the combined EVAG and CSμT to the given control commands, u_{EVAG} and $u_{CS\mu T}$.

$$\frac{d\left(\Delta\tilde{P}_{EVAG}(t)\right)}{dt} = \frac{-K_{EVAG}}{R_{EVAG}.\tau_{EVAG}}\Delta\tilde{f}_{IMG}(t) - \frac{1}{\tau_{EVAG}}\Delta\tilde{P}_{EVAG}(t) + \frac{1}{\tau_{EVAG}}u_{EVAG}(t-\delta_i). \tag{22}$$

Similarly,

$$\frac{d\left(\Delta\tilde{P}_{CS\mu T}(t)\right)}{dt} = -\frac{1}{\tau_{S\mu T}}\Delta\tilde{P}_{CS\mu T}(t) + \frac{\tau_{FA}-K_{S\mu T}}{\tau_{FA}.\tau_{S\mu T}}\Delta\tilde{P}_{FA}(t) + \frac{K_{S\mu T}}{\tau_{FA}} - \left(R^{-1}.\tau_{VA}\right)\Delta\tilde{f}_{IMG}(t) - \frac{1}{\tau_{VA}}\Delta\tilde{P}_{VA}(t) + \frac{1}{\tau_{VA}}u_{CS\mu T}(t-\delta_i) + \frac{\sum K_{i-ST}}{\sum \tau_{i-ST}}\Delta\tilde{P}_{ST}(t) \tag{23}$$

where δ_i is a time delay that changes over time and satisfies

$$0 \le \delta_i(t) \le \partial_i, \quad \frac{d(\delta_i(t))}{dt} \le \vartheta_i \le 1 \quad i = 1, 2, \ldots .n \tag{24}$$

where ∂_i and ϑ_i denotes the upper range and the variable rate of delay, respectively. In order to safeguard system operation, the measurement data, from all the distributed energy resources (DERs), is communicated to the microgrid power management system (PMS) of the IMG via a communication network. Based on the received data and error signal, the PMS decides the generation output of each DER and communicates the decision to each DER via the communication network. Since DER is distantly placed within the IMG, communication delay is unavoidable for the information exchange within the network. The communication delay is represented by the $G_D(s)$ Pede fifth-order approximation [36] in the form of a transfer function as follows:

$$G_D(s) = \frac{-\delta^5 s^5 + k_5\delta^4 s^4 - k_4\delta^3 s^3 + k_3\delta^2 s^2 - k_2\delta s + k_1}{-\delta^5 s^5 + k_5\delta^4 s^4 - k_4\delta^3 s^3 + k_3\delta^2 s^2 - k_2\delta s + k_1} \tag{25}$$

where $k_1 = 30240$, $k_2 = 15120$, $k_3 = 3360$, $k_4 = 420$, and $k_5 = 30$ are the factors of delay $G_D(s)$.

The following is how the state-space equations are expressed from (20) and (21):

$$\begin{cases} \dot{x}(t) = L.x(t) + H'.u_{CS\mu T}(t-\delta_i) \\ \qquad + H'_{EA}.u_{EVAG}(t-\delta_i) F.\Delta\varepsilon(t) \\ \Delta\tilde{f}_{IMG}(t) = J.x(t) \end{cases} \tag{26}$$

where the matrices H' and H'_{EA} can be illustrated as follows:

$$H' = \left[0 \quad 0 \quad 0 \quad \frac{1}{\tau_{VA}} \quad 0 \quad 0\right]^T$$

$$H'_{EA} = \left[0 \quad 0 \quad 0 \quad 0 \quad 0 \quad \frac{1}{\tau_{EVAG}}\right]^T. \tag{27}$$

From (14), the steady-state equations are as follows:

$$\begin{cases} \Delta\tilde{f}^{ss}_{IMG} = \lim\limits_{s\to 0} s\Delta\tilde{f}_{IMG} = \Delta\tilde{P}^{ss}_{Eq} - \Delta\tilde{P}_L \pm \Delta\tilde{P}^{ss}_{EVAG}\Big/\zeta(0) \\ \Delta\tilde{P}_{Eq}(s) = \left(\Delta\tilde{P}_{DFIG-WT}(s) + \Delta\tilde{P}_{CS\mu T}(s)\right); \\ \Delta\tilde{P}^{ss}_{CS\mu T} = \lim\limits_{s\to 0} s\Delta\tilde{P}_{CS\mu T}; M_{Eq}(s) \\ \qquad = M_{DFIG-WT}(s) + M_{CS\mu T}(s) \\ \Delta\tilde{P}^{ss}_{Eq} = \lim\limits_{s\to 0} sM_{Eq}(s) + \Delta\tilde{P}_{Eq}(s); \Delta\tilde{P}^{ss}_{EVAG} \\ \qquad = \lim\limits_{s\to 0} sG_D(s)\Delta\tilde{P}_{EVAG}.\zeta(0) \\ \text{and } \zeta(0) \approx D + R^{-1} \end{cases} \tag{28}$$

To modify the step load,

$$\Delta\tilde{P}_L(s) = \Delta\tilde{P}_L\Big/s. \tag{29}$$

In a steady-state scenario, both the frequency deviation and the RoCoF equal zero.

$$\Delta\tilde{f}^{ss}_{IMG} = 0. \tag{30}$$

From (28) and (30)

$$\Delta\tilde{P}_{CS\mu T} + \Delta\tilde{P}_{DFIG-WT} - \Delta\tilde{P}_L \pm \Delta\tilde{P}_{EVAG} = 0. \tag{31}$$

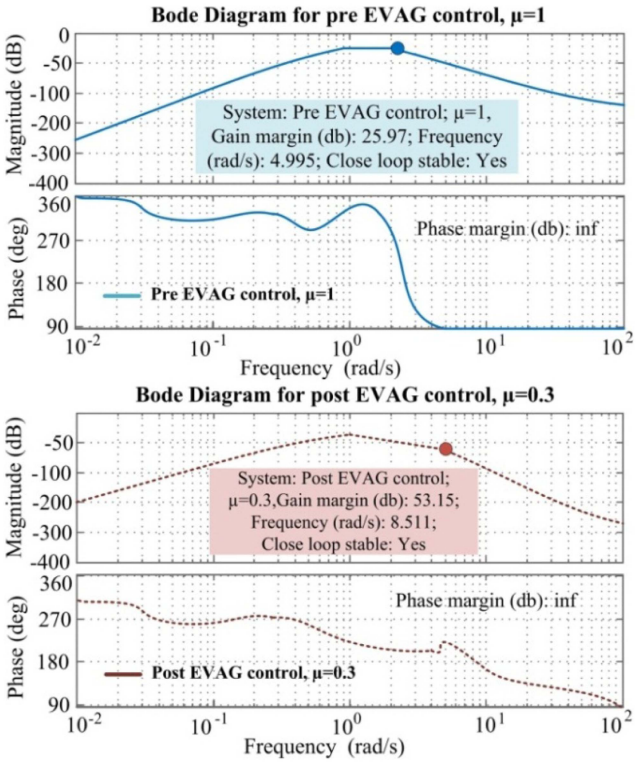

FIGURE 3. Comparative stability assessment under pre- and post-EVAG control.

Therefore, until the participation from the EVAG regulatory loop and secondary frequency regulation (SFR) exist, the steady state error for IMG's frequency stabilization events will never nullify (27). However, EVAG provides further assistance to strengthen LFR's activities. In order to smoothly maintain the system dynamics, the power-sharing between the EVAG loop and SFR loop plays a vital role to maintain a balance between the total power produced and the load demand. Hence, the EVAG power share being a part of LFR further demonstrates the LFR's strength. Furthermore, the SFR will offer the necessary oversight to maintain supply and demand in balance. Therefore, SFR and EVAG control effort (Λ) can be expressed as follows:

$$\left\{\Delta\tilde{P}_{Eq}^{ss} = \mu\Lambda \text{ and } \Delta\tilde{P}_{EVAG}^{ss} = (1-\mu)\,\Lambda. \right. \tag{32}$$

F. IMPACT ANALYSIS OF EVAG ON STABILITY

Based on traditional control concepts [35] the loop-based control system's stability is prerequisite to operate satisfactorily. To evaluate the stability of the test system under consideration in Fig. 2 two scenarios have been considered. First, the stability of the IMG test system is examined for traditional LFR, with $\mu = 1$ (no EVAG share), and then for LFR with EVAG framework, with $\mu = 0.3$. In order to assess the stability of the considered IMG system for centralized LFR and centralized LFR with EVAG share, stability assessment has been carried out using the Bode graph. The Bode graphs in Fig. 3 for both scenarios demonstrate their usefulness in calculating the gain as well as phase margins. It can be seen from Fig. 3 that, both situations showed an infinite phase margin (PM), with gain margins (GM) of 25.97 and 53.15 dB for $\mu = 1$ and $\mu = 0.3$, respectively. The comparative stability of the IMG test system is enhanced as the GM and PM rise, demonstrating an increasingly stable system. Fig. 3 shows how the test system's GM and PM significantly rise as a result of accounting for EVAG regulation in centralized LFR to improve the test power system's stability. Table 3 lists the eigenvalues of the system under investigation both post- and pre-EVAG control.

TABLE 3. Eigen Values of Islanded Test Microgrid System

Scenarios	Eigen values
Pre-EVAG control, (μ=1)	*−28.254 + 0.0000i, −23.027 + 4.519i, −12.625 + 0.0000i, −12.625 − 0.0000i, −0.318 + 0.0000i, −0.318 − 0.0000i, −1.481 + 0.0000i, 1.481 − 0.0000i, −1.481 + 0.0000i, −0.0971 + 0.0000i, −0.7137 + 0.0000i, 0.685 + 0.0000i, 0.000 + 0.0000i*
Post-EVAG control, (μ=0.3)	*−35.954 + 0.0000i, −20.177 + 18.473i, 20.177 − 18.473i, −22.674 − 21.404i, −22.674 − 21.404i, −31.273 + 0.0000i, −14.208 + 7.3729i, 14.208 − 7.3729i, −1.133 + 6.137i, −1.133 − 6.137i, −1.481 + 0.0000i, 1.481 − 0.0000i, −6.387 + 0.0000i, 2.405 + 0.0000i, −0.1004 + 0.0000i, 0.0659 + 0.0000i, −0.000 + 0.0000i, − 0.000 − 0.0000i,*

III. PROPOSED FRC AND PROBLEM STATEMENT

A. PRINCIPLE OF PROPOSED FUZZY RULE BASED TDOF-FTI WITH PR CONTROLLER

The suggested control system starts working by figuring out the μCE, which measures the frequency fluctuation on corresponding to the mismatched power between net generations and load. The suggested fuzzy rule based TDOF fractional order-tilt integral (FR-TDOF-F-TI) control technique with proportional resonant (PR) is based on the concepts of μCE, which is further utilized. The following stages can be used to explain this controller strategy.

Stage 1: In order to produce the output signal u_{FR} displayed in Fig. 4, the estimated μCE (γ_{IMG}) and its derivative ($\dot{\gamma}_{IMG}$) are supplied to a fuzzy rule (FR) based control. In the fuzzification process, the inputs $\gamma \in \{\gamma_{IMG}, \dot{\gamma}_{IMG}\}$ are fuzzified using a triangle membership function ($\eta(\gamma)$).

$$\eta(\gamma) = \begin{cases} 0, & \text{if } \gamma \le \eta_a \text{ or } \gamma \ge \eta_c \\ (\gamma - \eta_a)/(\eta_b - \eta_a), & \text{if } \eta_a \le \gamma \le \eta_b \\ -(\gamma - \eta_c)/(\eta_c - \eta_b), & \text{if } \eta_b \le \gamma \le \eta_c \end{cases} \tag{33}$$

where coordinate points $\{\eta_a, \eta_b, \eta_c\}$ are used to calculate the slope and capture of $\eta(\gamma)$. The Mamdani fuzzy interface engine [10], which is used to generate decision-making based on the criteria outlined in Fig. 4 (pale turquoise color), utilizes five linguistic variables: NB (negative big), NS (negative small), Z (zero), PS (positive small), and PB (positive big)

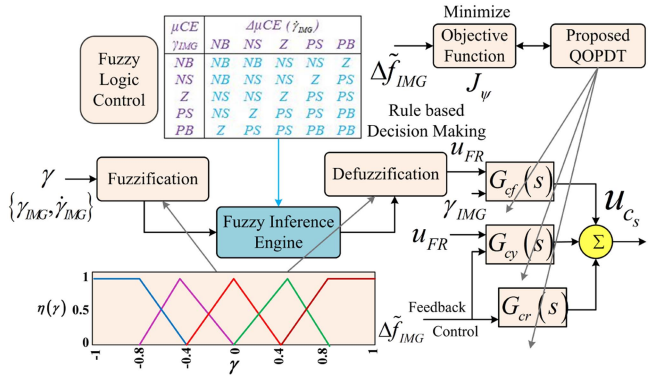

FIGURE 4. Representation of proposed control technique.

are utilized. Utilizing the centroid approach and a continuous membership function $\eta(\gamma)$, the defuzzification procedure is then applied after deciding to generate the u_{FR} control signal.

$$u_{FR} = \int \gamma\, \eta(\gamma)\, d\gamma \Big/ \int \eta(\gamma)\, d\gamma. \tag{34}$$

The suggested fuzzy rule-based method has the ability to tweak the coefficients, as well as higher accuracy with disturbance rejection abilities. A little bit longer run time for the control parameter's optimization may be one of the restrictions of FR based control approach.

Stage 2: In traditional single DOF controllers, the set-point response is frequently sacrificed when the disturbance response is optimized. With the additional degree of freedom provided by TDOF control systems, disturbances may be quickly rejected with enhanced set-point tracking which reduces higher overshoot of the system dynamics. In spite of that, integer-order (IO) control [37] improves certain performance metrics, FOC approach, including Fractional Order Tilt-integral (FTI) controllers, is preferred because of their resilience, greater tuning possibilities, effective responses in fractional order dynamics, and augmented transient as well as steady-state responses. Considering the pros of the fractional order (FO) of the Laplace variables, the FO integral differentiator operator S_{FI} can be written as follows [38]:

$$S_{FI} = \begin{cases} s^{\xi_m}, & R_E(\xi_m) > 0 \\ 1, & R_E(\xi_m) = 0 \\ s^{-\xi_m}, & R_E(\xi_m) < 0 \end{cases} \tag{35}$$

where $R_E(\xi_m)$ stands for the real component of ξ_m and ξ_m is a FO term. The definition of FO calculus by Caputo [38] states that $\xi_m : n-1 < \xi_m \leq n$, where $n \in R^+$. Nonetheless, in this study for effective system dynamics, the coefficient ξ_m is tuned in the range of (0–1). For practical application, a fifth-order Oustaloup filter [39] in the band-restricted frequency range $(10^{-3}, 10^{+3})$ can be utilized to effectively fit FO components. The output signal of FR-based control is received by the TDOF-FTI controller. The FR-based TDOF-FTI approach, which offers a more accurate and adaptable control mechanism, is produced by combining the natural adaptability of FR-based control and the mathematical sturdiness of the FTI controller. When assimilated with the TDOF control structure, this FTI control approach is capable of handling a wider range of operational situations with system uncertainties.

Stage 3: Finally, the overall microgrid's output, i.e., $\Delta\tilde{f}_{IMG}$ serves as a feedback controller via proportional resonant (PR) enables dynamic modification in reaction to the system uncertain disturbances. The inclusion of this feedback PR control is essential since it augments system stability and achieves desired performance. The benefits of PR include less complicated tuning and a greater disturbance attenuation ratio. The utilization of a proportional-resonant (PR) controller offers the benefit of achieving an infinite gain precisely at the resonant frequency, thereby guaranteeing the attainment of zero steady-state error at this particular frequency.

Now, the suggested FR-TDOF-FTI-(PR) controller output u_{c_s} can be represented as (34).

$$\begin{aligned} u_{c_s} = u_{FR}\Big[&\left(w_{ts}.\gamma_{IMG} - \Delta\tilde{f}_{IMG}\right)k_{ps} \\ &+ \left(\gamma_{IMG} - \Delta\tilde{f}_{IMG}\right).{}^{k_{is}}\!/_{s^{\varphi s}}\Big] \\ &- k_{ts}\left({}^{1}\!/_{s^{N_t^{-1}}}\right)\cdot\Delta\tilde{f}_{IMG} - \left(\Delta\tilde{f}_{IMG}\right).{}^{k_{Is}}\!/_{s^{\beta s}} \\ &- \left(\frac{2k_r s}{s^2+\varpi^2}\right).\Delta\tilde{f}_{IMG} \end{aligned} \tag{36}$$

where w_{ts} is the weight of tilt gain k_{ps}. The coefficients k_{Is}, β, and N_t are the fractional integral gain, fractional integral power factor, and tilt coefficient for the suggested controller. The parameter "k_r" denotes the gain associated with both the proportional and resonant components at the resonant frequency represented by "ω." The suggested controller as (36) can be accurately modeled by the FR-based output u_{FR} with μCE signals γ_{IMG} and $\Delta\tilde{f}_{IMG}$, which can be confirmed by Fig. 4.

$$u_{c_s} = u_{FR}.\gamma_{IMG}.G_{cf}(s) + \left(G_{cr}(s) + u_{FR}.G_{cy}(s)\right)\Delta\tilde{f}_{IMG} \tag{37}$$

where $G_{cf}(s)$ and $G_{cy}(s)$ are the feedforward and feedback components of the TDOF-FTI controller, respectively, and $G_{cr}(s)$ are the PR control components of the proposed controller.

The proposed designed FR-based TDOF-FTI controller with PR control enhances system robustness in the face of disturbances and uncertainties, provides versatility across a spectrum of linear and nonlinear control scenarios via fractional computations, enhances the accuracy of reference trajectory tracking, and proves highly suitable for real-time control applications owing to its streamlined implementation and minimal computational requirements.

B. OBJECTIVE ERROR FUNCTION FOR CONSTRAINTS OPTIMIZATION

In order to achieve optimum values for controllers' parameters, the primary objective is to reduce the system dynamics across a time horizon, such as frequency fluctuation $(\Delta\tilde{f}_{IMG})$,

in the IMG system. The objective error function J_ψ in (38) takes performance matric integral time multiplied absolute error (ITAE) into account to minimize the $\Delta\tilde{f}_{IMG}$ of the suggested controller.

$$J_\psi = \int_0^{T_{sim}} \left(\sum_{i=1}^{n} t \times \left| \Delta\tilde{f}_{IMG} \right| .dt \right) \tag{38}$$

subject to (s.t) $-0.15 \leq \Delta\tilde{f}_{IMG} \leq 0.2$ with simulation run time of T_{sim}. For the proposed FR-TDOF-FTI-PR controller the values of parameters $O_{jr} \in \{w_{ts}, k_{ps}, k_{is}, \varphi_s, k_{ts}, N_t, k_{Is}, \beta, k_r\}$leveraged to estimate $\Delta\tilde{f}_{IMG}$via the proposed controller can be attained by the algorithmic technique described in Section V.

C. PROPOSED QOPDT

The PDT method, introduced by Ezugwu et al. [27] in 2022, draws inspiration from the behavioral patterns observed in prairie dogs, a rodent species predominantly inhabiting the deserts of North America. Prairie dogs, resilient inhabitants of some of the most rugged terrains on the planet, possess adaptive traits such as robust limbs, elongated claws, and rapid short-distance locomotion, facilitating evasion from predators and sheltering within interconnected burrow systems when threatened.

As social animals, prairie dogs organize into extensive colonies comprised of smaller units known as "coteries," fostering collective resource sharing and communication mechanisms, including foraging signals and predator alerts. The PDT methodology delineates two primary phases, namely exploration, and exploitation, mirroring the foraging behavior and burrow construction activities of prairie dog communities, respectively, and their responses to communication cues. Global algorithmic approaches such as the differential evolution technique (DE), PSO technique, grasshopper algorithm (GOA) technique, and PDT demonstrate proficiency in generating optimal or near-optimal solutions, their suitability may diminish when applied to problems characterized by minimal dimensional complexity and few fitness evaluations or for those with high dimensional complexity and numerous fitness evaluations. In these scenarios, the application of algorithms such as the QOBL solution is recommended. The success of most global optimization algorithms largely depends on the fine-tuning of specific control parameters, which critically influence their convergence characteristics. As an illustration, pivotal elements within the DE algorithm encompass the crossover rate (Cr) and scaling factor (sf), while the PSO method relies on parameters such as the inertia weight (w), social parameter (c_1), and cognitive parameter (c_2). Similarly, the GOA technique hinges on factors such as the intensity of attraction (I_A) and attractive length (AL). In contrast, the PDT approach necessitates only a singular control parameter, thereby streamlining its application, enhancing adaptability, and bestowing the advantages of being free from derivative computations and operationally efficient. This simplicity has spurred widespread adoption of the PDT methodology among researchers across diverse domains. Consequently, this algorithm has been benchmarked against various standard power system benchmark problems to assess its performance both quantitatively and qualitatively compared with other optimization methods [27]. However, significant enhancements in PDT's performance could be realized by integrating it with the QOBL operator, resulting in a hybrid QOPDT configuration. Further follow-up analysis has revealed that the QOBL solution has a striking impact on global optimums, in stark contrast to both random and opposing solutions. The QOPDT exhibits the following distinctive characteristics.

i) It enhances initial population diversity and productivity by incorporating the QOBL operator throughout the iterative process.
ii) The method effectively avoids premature convergence and entrapment in local optima.
iii) By integrating the QOBL operator with prairie dog movement patterns, rather than relying on a uniform distribution, QOPDT achieves an optimal balance between exploration and exploitation phases, thereby enhancing solution precision.

The following stages outline the process for implementing the solution to the assignment.

Initialization phase: The foraging behavior of each prairie dog is depicted as a $1 \times$ dim spatial dimension. To ensure that prairie dogs do not stray from their intended foraging paths, upper-bound (*ub*) and lower-bound (*lb*) constraints are established to confine their range of movement. The positioning of each prairie dog at various locations represents a potential solution to the problem.

Exploration phase: During the initial time period, the positioning of prairie dogs in their foraging behavior was influenced by the proximity to food sources "*c*," the current food quality, and the positions of artificially generated prairie dogs. In the mathematical model, the current food quality is defined in terms of the effectiveness of the best solution currently evaluated, expressed as "ep_{best}." Additionally, the location of a synthetically created prairie dog is characterized by the random cumulative effect, labeled "$CPD_{i,j}$." The respective calculation formula is presented as follows:

$$\begin{cases} ep_{best\,i,j} = g_{best\,i,j} \times \Lambda + \left(\frac{PD_{i,j} \times mean(PD_i)}{g_{best\,i,j} \times (ub_j - lb_j) + \Lambda} \right) \\ \Rightarrow CPD_{i,j} = \frac{g_{best\,i,j} - rand.PD_{i,j}}{g_{best\,i,j} + \Lambda} \end{cases} \tag{39}$$

where $g_{besti,j}$ is the best global solution attained to date, Λ represents small variances among prairie dogs, and $rand.PD_{i,j}$ are random positions. The updated formula for prairie dog foraging positions is

$$PD_{i+1,j+1} = g_{best\,i,j} - ep_{best\,i,j} \times c - CPD_{i,j} \times Levy\,(n)\,. \tag{40}$$

In (40), Levy refers to a levy distribution characterized by discontinuous jumps. Upon locating new food sources, prairie dogs commence digging and constructing new burrows in the vicinity. During this phase, the positioning of prairie dogs correlates with their digging strength, denoted as "D_S," at these

sites. The formula to update D_S and $PD_{i+1,\,j+1}$ is outlined as follows:

$$\begin{cases} D_S = {}^{3}\!/_{2} \times rand \times \left(1 - t/t_M\right)^{\left(2^{t}/t_M\right)}; \quad rand \in \{-1, 1\} \\ \Rightarrow PD_{i+1,\,j+1} = g_{best\,i,j} \times randPD \times D_S \times Levy\,(n) \end{cases}. \tag{41}$$

Exploitation phase: In the third and fourth time period, prairie dogs consider the quality of the current food source, ε, and the collective impact of all prairie dogs to randomly update their positions. In the mathematical formulation, "ε" is defined as a small number indicative of food source quality. The position update formula for prairie dogs followed by predator effect (P_E) is specified as follows:

$$\begin{cases} PD_{i,j} = g_{best\,i,j} - ep_{best\,i,j} \times \varepsilon - CPD_{i,j} \times rand \\ P_E = {}^{3}\!/_{2} \times \left(1 - t/t_M\right)^{\left(2^{t}/t_M\right)} \\ PD_{i,j} = g_{best\,i,j} \times P_E \times rand \end{cases}. \tag{42}$$

The noteworthy QOPDT is created by combining PDT with the QOBL paradigm in order to enhance PDT's performance. The mathematical formulations for Oppositional-based learning (OBL) and QOBL are represented in (44)–(46).

In the context of a one-dimensional search space bounded by the real numbers s and r, let k be a real number within this range. The opposing number k_o is defined as the mirror image of k, with the following specification:

1) OPPOSITE NUMBER

$$k_o = s + r - k \tag{43}$$

where k signifies a randomly initialized value, and s and r denote the population's two extreme points. Analogously, for a d-dimensional search space, the concept of an opposing population is articulated as follows:

2) OPPOSITE POINT

$$k_{o,p} = s_p + r_p - k_p \tag{44}$$

where $k_p \in \{s_p, r_p\},\ p = 1, 2, \ldots d$

3) QUASI-OPPOSITIONAL (QO) SOLUTION IN D-SPACE

$$k_{o,p} = s_p + r_p - k_p \tag{45}$$

$$k_{qo,p} = rand\left({}^{s_p + r_p}\!/_{2}, k_{p,o}\right) i.e.,\ p = 1, 2, ..d. \tag{46}$$

The stepwise QOPDT technique is shown in Algorithm 1.

The proposed QOPDT's pseudo code is provided in the following. In order to test the performance of the proposed QOPDT some benchmark function, i.e., single peak (F_1-F_7) and multimodal (F_8-F_{12}) functions [27], depicted in Table 4 are tested by QOPDT, basic PDT, and PSO considering the dimension of 50 and iteration (t_M) of 100. The statistical "*Avg*," "*Std*," and "*evaluation time* (E_T)" values under different functions have shown that the performance of QOPDT is better than PDT and PSO. To assess the effectiveness of the proposed QOPDT algorithmic technique, the Figure of Demerit (FOD) is compared with the most recent PDT technique as well as to other algorithmic techniques such as PDT [27], QOHHO [24], and C-BO [15]. The convergence plot is shown in Fig. 5, which amply proves the superiority of the proposed QOPDT. The overall methodological framework of the proposed work is depicted in Fig. 6.

Algorithm 1: Proposed QOPDT.

Input: Initialized no of prairie dog (PD) n_i *(i=1, 2, …X),* maximum iteration (t_M), number of coteries (m), food source factors (c, ε),coteries in colony *(CC), ub and lb*

1: Create opposing and quasi-opposing populations centered within the search space using (43)–(46).
2: Compute the objective function of the QO population utilizing (38).
3: Execute the selection of the most suitable population from both the current and QO solutions.
4: Verify the positioning of the parameter's values for the controllers.
5: Set the inertia weight ω_i using $\omega_i = ub - ({}^{ub - lb}\!/_{t_M}) \cdot i$
6: Calculate the fitness of PD and find individual best solution (ep_{best})
7: Update the digging strength and predator effect (D_S, P_E) using
$\begin{cases} D_S = {}^{3}\!/_{2} \times rand \times (1 - t/t_M)^{(2^{t}/t_M)}; \quad rand \in \{-1, 1\} \\ P_E = {}^{3}\!/_{2} \times (1 - t/t_M)^{(2^{t}/t_M)} \end{cases}$
8: Update randomized cumulative effect of all PD (CPD_{ij})
9: Update position of prairie dog ($PD_{i,j}$) by
$\begin{cases} PD_{i+1,j+1} = g_{best_{i,j}} - ep_{best_{i,j}} \times c - CPD_{i,j} \times L'evy(n) \Leftarrow Foraging\ activities \\ PD_{i+1,j+1} = g_{best_{i,j}} \times ep_{best_{i,j}} \times DS \times Levy(n) \Leftarrow Burrowing\ activities \\ PD_{i+1,j+1} = g_{best_{i,j}} - ep_{best_{i,j}} \times \varepsilon - CPD_{i,j} \times rand \Leftarrow Food\ alarm \\ PD_{i+1,j+1} = g_{best_{i,j}} \times PE_j \times rand \Leftarrow Hunting\ alarm \end{cases}$
10: Calculate the fitness of individual beetle and update the individual and global best solution (p_{best}, g_{best})
11: Go to movement of prairie dog (PD) to update location
12: Update step size of iteration δ using $\delta^{t+1} = eta.\,\delta^{t}$
13: Generate QO population.
14: Decide whether to conclude the iteration process. If affirmative, output the global optimal solution derived from the quasi-oppositional population; otherwise, return to the third step.

Output Best value $\mathbf{g_{best}}$

TABLE 4. Comparison of Proposed Optimization Performance With Standard Benchmark Functions

Fn	QOPDT			PDT			PSO		
	Avg	*Std*	E_T	*Avg*	*Std*	E_T	*Avg*	*Std*	E_T
F_1	1.52	1.90	2.57	3.89	3.17	3.48	2.75	2.08	4.19
F_2	0.97	1.13	1.94	2.36	1.66	6.08	3.04	1.97	6.83
F_3	18.3	27.2	0.85	30.7	64.1	2.47	77.51	105.9	5.02
F_4	0.612	0.879	3.16	3.40	7.08	5.72	14.27	4.09	6.65
F_5	9.06	34.07	2.56	48.3	50.4	4.37	71.8	60.1	7.11
F_6	15.91	11.79	1.16	62.73	58.92	3.04	27.05	20.82	4.89
F_7	0.078	0.029	2.59	0.038	0.046	3.19	0.109	0.118	3.61
F_8	−12378	4135.1	0.97	−9836.4	2487.2	1.65	−6893.5	1328.7	2.73
F_9	23.486	11.39	1.07	29.78	27.01	1.94	40.87	31.72	2.48
F_{10}	0.870	0.967	1.58	1.864	5.319	2.08	7.012	1.137	2.94
F_{11}	3.056	0.463	1.26	9.331	14.08	2.34	4.053	0.767	3.01
F_{12}	0.623	0.378	3.53	2.047	2.249	4.28	14.701	7.931	4.68

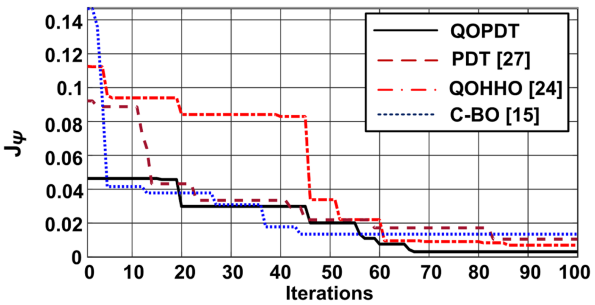

FIGURE 5. Comparative convergence plot of different techniques with proposed algorithmic technique.

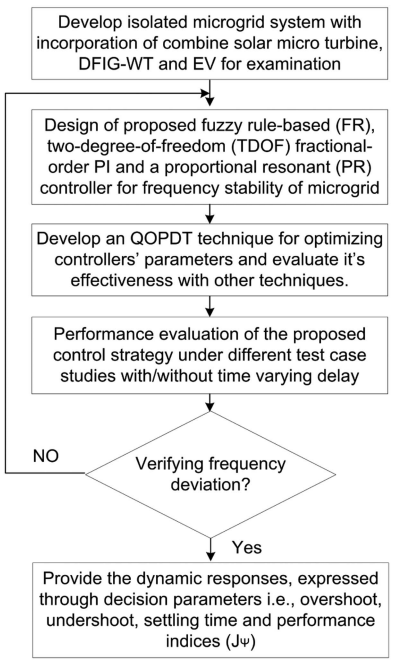

FIGURE 6. Overall methodological framework of the proposed work.

D. COMPUTATIONAL COMPLEXITY: PROPOSED QOPDT

The examined microgrid system comprises of multiple interconnected subsystems. Streamlining the control strategy's development and minimizing the computational burden entailed in its optimization process would be significantly advantageous, necessitating a linearized mathematical model. The computational workload is impacted by the interplay between processing time and problem scale within the methodology, thus justifying the adoption of the Big-$\tilde{\Re}$notation as a customary measure for this correlation. The intricacy of the approach is delineated by variables such as the number of dimensions (D_m), iterations counts (I_c), and the computational expense associated with function evaluation (F_E).

$$\tilde{\Re}_{(QOPDT)} = \tilde{\Re}\left(problem\,defination\right) + \tilde{\Re}\left(initilization\right) + \tilde{\Re}\left\{I_c\left(function\,evaluations\right)\right\} + \tilde{\Re}\left\{I_c\left(memory\,saving\right)\right\} + \tilde{\Re}\left\{I_c\left(position\,update\right)\right\}. \quad (47)$$

Therefore, to determine the overall computational complexity, the following equation can be utilized:

$$\Rightarrow \begin{cases} \tilde{\Re}_{(QOPDT)} = \tilde{\Re}(1 + D_m.N + I_c.F_E.N \\ \qquad\qquad + I_c.N + I_c.N.D_m) \\ \qquad\qquad \cong \tilde{\Re}\left(I_c.N.D_m + I_c.F_E\,.N\right) \end{cases}. \quad (48)$$

The complexity displays polynomial traits, thus suggesting that the QOPDT approach may be deemed an efficacious methodology.

IV. SYSTEM RESULTS AND DISCUSSION

A. TEST SYSTEM EXPLANATION WITH LABORATORY PLATFORM

To examine the system dynamics while accounting for the real load profile and RPG intermittency, an IMG is used as a test system. The IMG test system depicted in Fig. 2(a) includes the actual load data [40] and real recorded solar power variations provided by NASA, USA [33]. Physical restraints such as generation rate constraint (GRC) with 0.0005/s and G_D (s) are considered to make the targeted study more realistic. In the test IMG system DFIG-WT, CSμT generations have been considered with effective participation EVAG units. The IMG

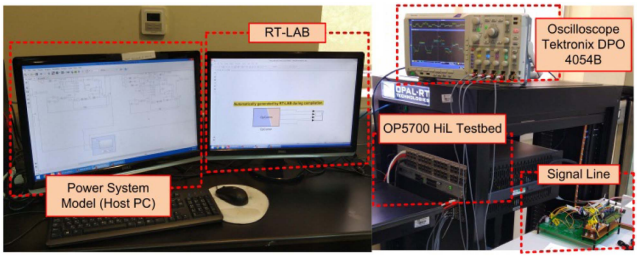

FIGURE 7. OP5700 Opal-RT setup for real-time experiment.

is operated here with a standard 50 Hz frequency with a capacity of 3 MW.

The applicability and dependability of the proposed control structure are assessed via hardware-in-loop (HiL) study. The real-time digital simulator (RTDS) despite offering effective HiL study, is less appealing due to its high price. In contrast, the dSPACE Tool Box struggles to accommodate high-fidelity models because of its slow sampling rate and constrained computing power. In order to resolve these challenges, this study chooses HiL validation on the Opal-RT (OP-5700) testbed, which includes both DSP and FPGA processors and satisfies our computational resource needs. This testbed runs on the MATLAB/Simulink Sim Power Systems-based RT-LAB software, which is renowned for advancing model-based design in electric power networks. The experimental architecture for the test microgrid system is depicted in Fig. 7. The following are illustrations of investigations done taking into account for various.

B. TEST CASE STUDIES

To determine the resilience of the suggested controller, five various test case studies are examined.

- Case study I: System dynamics during 10% load perturbation while RPG fluctuation.
- Case study II: Effectiveness of G2V and V2G operation on microgrid performance.
- Case study III: Performance analysis during real recorded intermittency in RPG and load.
- Case study IV: Sensitivity assessment of the proposed controller against parametric uncertainties.
- Case study V: Stability analysis.
- Case study VI: Assessment of time-varying delay in EVAG-based LFR framework.

Case study I: This case study is meant to demonstrate the effectiveness of the QOPDT-based proposed controller through performance evaluation of system dynamics with $\mu = \{1, 0.3\}$. In the present operating study, a 10% change in load demand is considered at $t = 2$ s onwards and the respective IMG frequency dynamics have been analyzed. Fig. 8(a) illustrates the frequency responses ($\Delta\tilde{f}_{IMG}$) under the operating conditions outlined in the case study I. The power sharing of CSμT and EVAG for the targeted LFR problem is depicted in Fig. 8(b) and (c). The system dynamics corresponding to "LFR with $\mu = 1$" and "LFR with $\mu = 0.3$" are clearly

TABLE 5. Optimized Controllers Under Case Study I Operating Conditions

Controllers' parameters	Optimized parameters without EVAG ($\mu = 1$)	Optimized parameters with EVAG ($\mu = 0.3$)
w_{ts}	0.017	0.129
k_{ps}	0.534	2.073
k_{is}	0.839	0.672
φ_s	0.438	0.941
k_{ts}	3.148	1.042
k_{Is}	2.593	1.749
N_t	48.35	41.04
β_s	2.738	2.105
k_r	3.072	2.728

displayed in Fig. 8 where analysis manifests that "LFR with $\mu = 0.3$" enhanced $\Delta\tilde{f}_{IMG}$ by 50.24% compared to "LFR with $\mu = 1$" and supports LFR service. Table 5 represents the QOPDT optimized designed controllers' coefficients for the case study I operating condition. Furthermore, the influence of "LFR with $\mu = 0.3$" against "LFR with $\mu = 1$" on dynamic $\Delta\tilde{f}_{IMG}$ response is evaluated through decision parameters such as maximum overshoot (OV_m), undershoot (US_m), and settling time (t_s) is presented through a bar graph as shown in Fig. 9.

Case study II: The integration of EVAG into microgrids significantly affects their performance, particularly during charging periods. EVs interact with the base microgrid in two principal modes: grid-to-vehicle (G2V) for battery charging, and vehicle-to-grid (V2G) for discharging the battery back into the grid. The operation of power electronics converters facilitates the charging or discharging of EV batteries from the microgrid. Typically, an EV enters the charging mode after extensive use or continuous operation, functioning simply as an additional load that draws power from the grid until the battery reaches its SoC limit. This integration scenario can lead to substantial deviations in microgrid frequency from its nominal value, prompting immediate intervention by controllers to mitigate frequency oscillations and restore stability.

Conversely, fully charged EVs can contribute electricity back to the microgrid under conditions of overloading or dynamic loads, enhancing overall power quality. In this instance, the presence of a secondary controller swiftly ensures the maintenance of the nominal frequency. Fig. 10(a) illustrates the frequency deviation experienced by the microgrid under three different EV operational modes. During EV charging (G2V), the frequency error response tends to oscillate more and stabilizes more slowly, indicating significant deviations under charging conditions. In contrast, when no EV is connected, the frequency variation occurs only due to step load changes and is relatively minor. However, in the V2G scenario, where the EV discharges into the grid, the frequency deviation is considerably reduced. Here, the EV acts in conjunction with the secondary controller as a stabilizing power source, effectively smoothing out frequency disturbances. Fig. 10(b) depicts the per unit output power of the EV battery under various conditions. Initially, for the first five seconds, there is no EV integration within the system. However, during the subsequent interval from five to twelve seconds, the

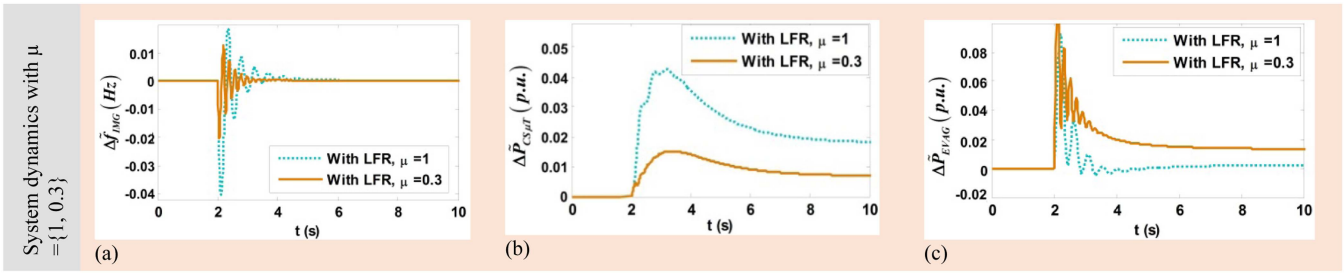

FIGURE 8. System dynamics with μ (a) frequency fluctuation in IMG, (b) change in power of CSμT, and (c) change in power of EVAG for case study I.

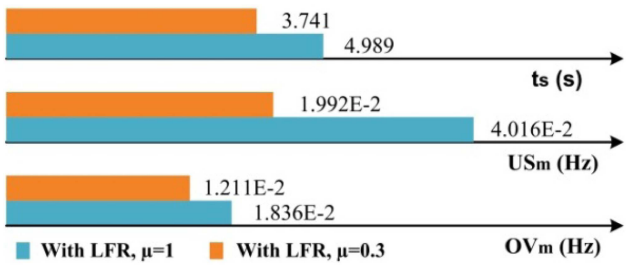

FIGURE 9. Bar chart illustrating the impact of parameter μ on dynamic test systems.

EV operates either in charging (G2V) or discharging (V2G) modes. In the V2G mode, the battery is capable of supplying power to the grid depending on the demands of the microgrid. Conversely, in G2V mode, the battery consumes power from the grid to recharge. A positive battery power value indicates power delivery to the grid (discharging), while a negative value signifies power consumption from the grid (charging). As the number of electric vehicles escalates, the charging power correspondingly increases. Fig. 10(c) illustrates the frequency fluctuations in the microgrid when multiple groups of EVs are charging, generated using the Simulink platform. An adaptive QOPDT-based FR-TDOF-FTI-(PR) controller is proposed to manage these dynamics. The findings suggest that the stability of the frequency response is adversely affected as more EVs are integrated into the grid. Fig. 10(d) presents the per unit output power of the CSμT during scenarios of EV charging and discharging. During the EV charging phase, the CSμT is required to supply more power compared with the discharging phase. Power variations in the CSμT are analyzed under step load disturbances of 2% and 4%. In the initial 12 s, where no EV is connected, the CSμT solely addresses the step load dynamics. Post 12 s, as the EV begins to interact with the IMG, the diesel generator adjusts its output to meet the evolving requirements. Throughout these transitions, the proposed FR-TDOF-FTI-(PR) controller effectively maintains stability and reliability in the CSμT's output power.

Case study III: This case study assesses the system dynamics of IMG during the real-time stochasticity in the RPG power fluctuation. The IMG dynamics are depicted in Fig. 11(a)-9(b), and the fluctuation of photovoltaic is displayed in Fig. 11 (c). However, Figs. 12(a)-10(c) correspondingly

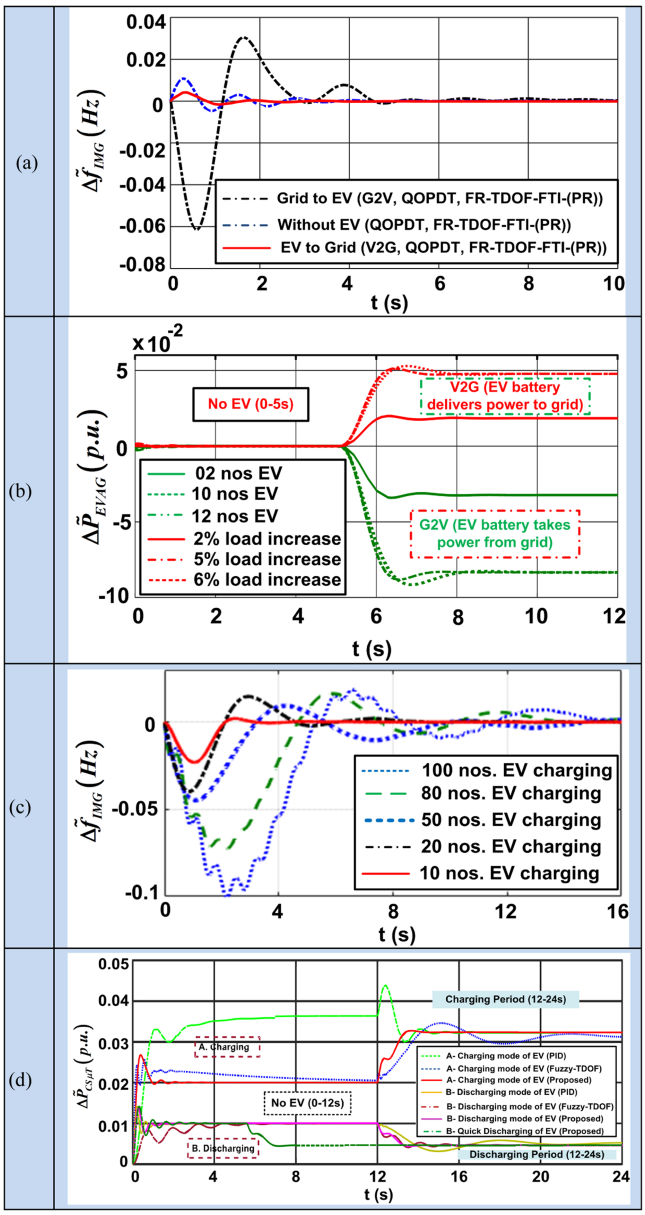

FIGURE 10. (a) Dynamic frequency response under various EV modes. (b) EV battery power sharing during different actions. (c) Frequency response within group of EVs. (d) CSμT output power.

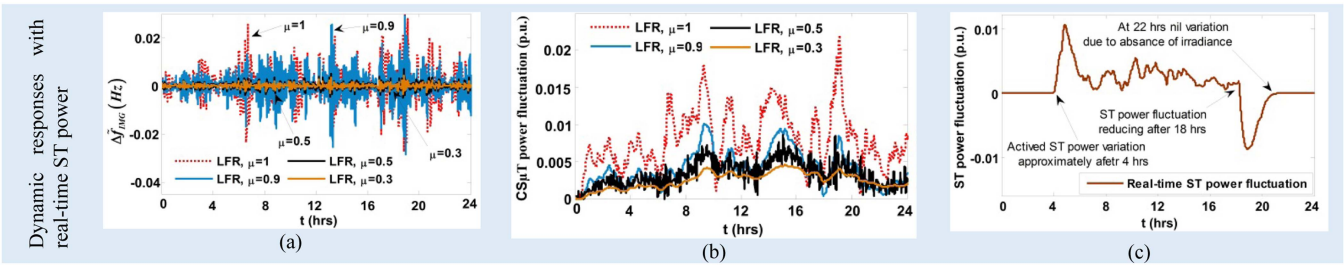

FIGURE 11. Dynamic responses with real-time ST fluctuation.

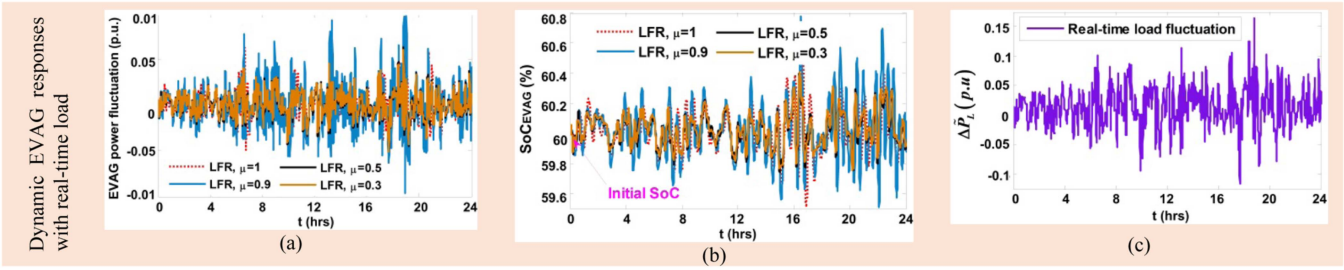

FIGURE 12. Dynamic EVAG responses with real-time load fluctuation.

depict the power sharing of EVAG, actual load variation and change in EVAG power in real time with its SoC. In this scenario, the LFR with different values has been considered in the operational test system.s event where the renewable solar generation and load demands. In order to assess the viability of the considered system, a real-recorded load data is taken from IEEE PES Load data where the variable solar power is obtained from NASA, USA. The resolution of these data is typically 5 min (288 samples each day). Upto 5% of net load demand is scaled as shown in Fig. 12 (c). The transient responses of the assessed IMG model for different (1, 0.9, 0.7 and 0.3) is given in Fig. 11 (a)-(b) and Fig. 12 (a)-(b) which demonstrates that the improved dynamics are defined for = 0.3 with 0.7 EVAG control

Case study IV: Sensitivity assessment is used in this case study to affirm that the proposed controller will continue to work even when IMG's coefficients and load demand are drastically changed in case study II. Moreover, it might be challenging to precisely estimate variables such as the inertia value (M) and damping factor (D) in a real microgrid power network. As a result, it is estimated that D and M have an indeterminacy of around ±30% with regard to their rated values. In order to conduct the study, IMG is measured against 30% parametric uncertainties in M and D, each taken individually, for the 70% EVAG support with the $\mu =$ 0.3 and the 50% EVAG support in frequency response with the $\mu = 0.5$, respectively. The evaluation of the system dynamics of the IMG in Fig. 13 demonstrates the robustness of the suggested control method in the face of significant changes to the system entity. Observations show that the proposed controller functions continuously and is exceptionally efficient in parametric uncertainties with significant IMG fluctuations.

Case study V: In the realm of feedback control systems, ensuring stability is essential for consistent operation. To assess linear stability, a Bode plot is utilized for the model depicted in Fig. 1. The Bode diagrams are instrumental in analyzing the stability of a power system when it integrates fuzzy TDOF, fuzzy fractional order proportional resonant (FOPR) controller, and proposed FR-TDOF-FTI-(PR) controller. Despite certain operational limitations, the system primarily demonstrates stable characteristics, as shown in Fig. 14. A key factor in this stability analysis is the gain crossover frequency, where the magnitude plot crosses the 0 dB line. This frequency is vital in determining the Phase Margin (PM), which, in the analyzed conditions, is effectively infinite due to the absence of a 0 dB crossover. Specifically, the phase crossover frequencies for the fuzzy TDOF and fuzzy FOPR control schemes are recorded at 1.193 and 2.185 rad/s, respectively. However, when the system is augmented with the proposed FR-TDOF-FTI-(PR), the phase crossover frequency notably increases to 2.716 rad/s. Furthermore, the proposed FR-TDOF-FTI-(PR) control scheme not only maintains the infinite phase margin but also enhances the gain margin, indicating a shift toward a more stable system configuration.

Case study VI: Mostly, for the purpose of triggering control signals, two-way communication between control devices and the control center frequently involves time-varying communication time delays. The performance of IMG's frequency is therefore examined in order to illustrate the effect of these time-varying delays on system dynamics. Fig. 15 shows the plotted result, using the identical dataset leveraged in case study III. The variable time delays (δ) are displayed in Table 6.

It is clear from the system dynamic response analysis that the time-varying delay $\delta = 10\text{sint} + 1.2$ s, represented by

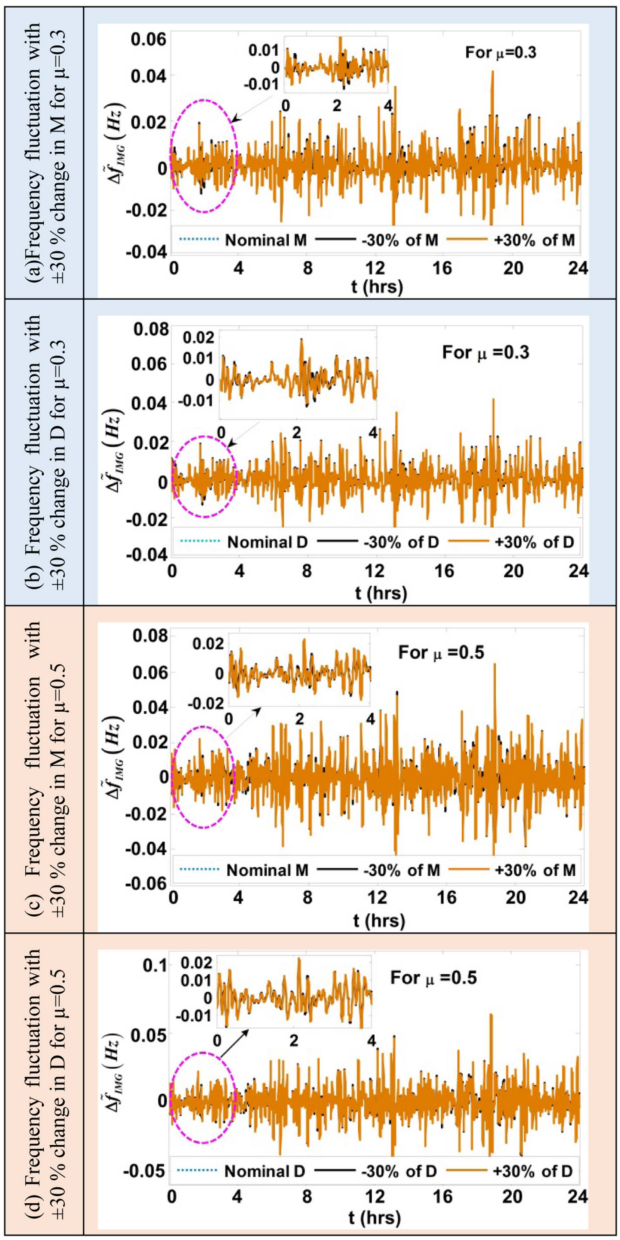

FIGURE 13. Dynamic responses under parametric uncertainties of IMG system.

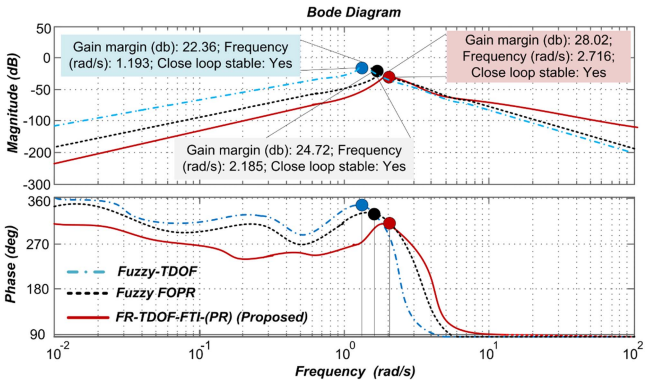

FIGURE 14. Comparative stability assessment of fuzzy-TDOF, fuzzy FOPR, and proposed FR-TDOF-FTI-(PR) control schemes.

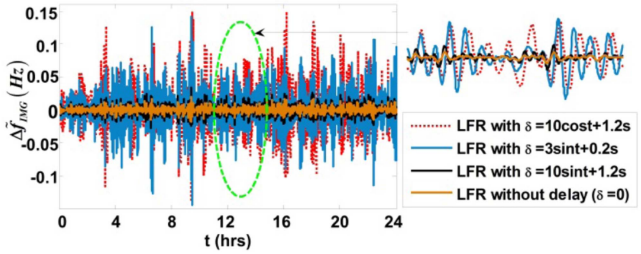

FIGURE 15. IMG's frequency fluctuation associated with different time-varying delays in the LFR framework.

TABLE 6. Maximum Frequency Fluctuation Under Various Time-Varying Delays

Time-varying delay "δ"	Max^{m} frequency fluctuation for proposed controller within 24 h, Hz
Without delay, δ = 0	0.0246 Hz
δ = 10cost + 1.2 s	0.1473 Hz
δ = 3sint + 0.2 s	0.1409 Hz
δ = 10sint + 1.2 s	0.0328 Hz

the yellow line, has far less instances of dips and peaks in$\Delta\tilde{f}_{IMG}$. The pale turquoise line indicates a time-varying delay $\delta = 10\text{cost} + 1.2$ s, which results in more pronounced deviations. The significance of the effect of variable time delay in the EVAG and CSμT on microgrid frequency response is shown by this observation. It follows that a quicker and more efficient communication arrangement is required to efficiently collect and transfer real-time data between the central control unit and the smart meters deployed on EVAG/CSμT appliances. With such a system in place, frequency changes might be responded to promptly and precisely, assuring the reliable action of power network.

According to the analysis shown in Fig. 15, the system dynamics display outstanding performance in conventional LFR merged with EVAG/CSμT with no time-varying delay $\delta = 0$. However, as time-varying delay is incorporated, the system frequency response starts to deviate. Notably, the test findings demonstrate that the proposed control strategy employing time-varying delay $\delta = 10\text{cost} + 1.2$ s, put out in this study can keep frequency fluctuation to a maximum of 0.15 Hz. This demonstrates the advantages of the microgrid system with the proposed FR-TDOF-FTI-(PR) control strategy. As a result, an investigation is done in relation to the test IMG system taking into account a value of $\mu = 0.3$, and it is shown that the response is better under time-varying delay $\delta = 10\text{sint} + 1.2$ s.

C. COMPARATIVE PERFORMANCE ANALYSIS

This investigation assesses the proposed controller's adaptability to changes in controller properties in the IMG system under circumstances of time-varying delay in the LFR. In order to evaluate the effectiveness of the suggested control action with time-varying communication delay

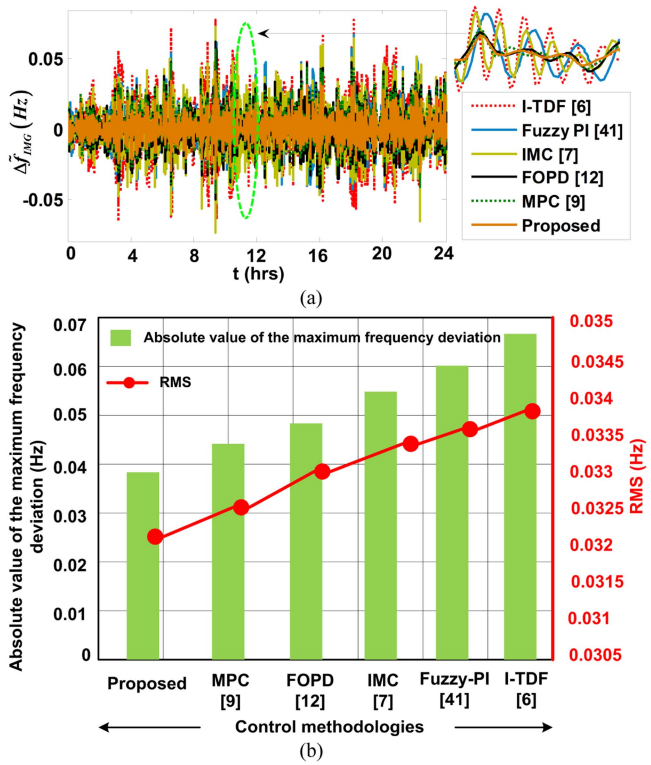

FIGURE 16. (a) Comparative frequency fluctuations of microgrid test system under different published control methodologies with real-time power variations of ST and load variation. (b) Bar graph illustration of performance evaluation under proposed control method against preexisting control methodologies.

TABLE 7. Comparative Computational Complexity for Different Control Strategies

Control strategies	Computational time (s)	Control update numbers
Proposed	4089	869
MPC [9]	4203	1548
FOPD [12]	5175	3279
IMC [7]	4631	2015
Fuzzy PI [41]	4708	1278
I-TDF [6]	4365	3108

$\delta = 10\sin t + 1.2$ s, Fig. 16 shows the comparative analysis of scenario III with actual demanded load and RPG fluctuation. Notably, case study III disregards a time-varying delay in the LFR framework. It is evident from Figs. 11 and 12 of case study III, the recommended control technique responds better to the frequency fluctuation for $\mu = 0.3$, taking 70% EVAG regulation into consideration. As a result, in this scenario, the suggested controller's ability to prevent an unconstrained time-varying delay in the secondary control loop with $\mu = 0.3$ is evaluated using the I-TDF [6], Fuzzy PI [41], internal model control (IMC) [7], FOPD [12], and MPC [9] control methodologies. Whereas comparing the dynamic response of the proposed control technique, peak deviations and computational time are crucial parameters that show the effectiveness of the controller. The computational time and control update numbers for different control schemes are depicted in Table 7. Fig. 16 and Table 7 compare the efficacy and adaptability of the suggested control approach to those of pre-existing control strategies. It is clear from this comparison that the proposed control strategy outperforms the other robust scheme in the IMG in terms of improving the frequency stabilization mechanism and is more resilient to the occurrence of time-varying delay oscillation.

TABLE 8. Pros and Cons of Suggested Frequency Stabilization Scheme

Pros	Cons
1. Simple to realize, adaptable, and robust (owing to a higher degree of freedom and integration of fuzzy rule-based approach)	1. A linearized isolated MG system has been taken into consideration to evaluate the proficiency of the controller
2. Higher disturbance rejection capability and effective tracking performance due to closed-loop multilayer control structure	2. Computationally intensive
3. Integration of quasi-oppositional learning and Foraging movements behavior in prairie dog technique (MPT) enhances convergence mobility and avoids premature solutions	3. The considered PDT performance depends on the best selection of two input factors i.e., m, ε
4. Dynamic responses are enhanced adequately in the viewpoint of frequency deviation, convergence characteristics, and performance parameters	

V. CONCLUSION

This work offers a number of novel contributions, with a primary emphasis on incorporating EVAG into LFR and switching from conventional microturbine generation adjustments to CSμT for effective frequency management. It conducts a thorough investigation of the effect of EVAG control on the test IMG power system's transient behaviors while accounting for the stochastic nature of the real-time RPG and load. A novel fuzzy rule-aided FOC stratagem is proposed for a TDOF-FTI-(PR) controller, optimizing together transient and steady-state system dynamics, leading to robust and accurate control performance. The study employs a proposed QOPDT technique to improve the ITAE error function, significantly enhancing the proposed controller's overall responses and system stability. It is discovered that the minimum ITAE is 0.00461 for QOPDT, 0.00927 for QOHHO, 0.01283 for PDT, and 0.01449 for C-BO. This study offers a practical method for preserving the balance between supply and demand as renewable sources are widely installed in microgrid power networks. To further examine the dynamic responses of the test system, the natural time-varying delay is taken into account within the LFR framework. The comparative frequency response with time-varying delay shows that the IMG test system applying the proposed control strategy enhanced by 97.82%, 91.27%, 86.95%, 71.73%, and 69.43%, respectively, compared with I-TDF, IMC, fuzzy-PI, FOPD, and MPC control mechanisms. Table 8 summarizes the pros and cons of the suggested control mechanism. In order to confirm the viability of the suggested technique for erratic sources and loads, the

research also offers an experimental evaluation utilizing the OP-5700 Opal-RT platform.

ACKNOWLEDGMENT

The statements made herein are solely the responsibility of the authors.

REFERENCES

[1] M. H. Rehmani, M. Reisslein, A. Rachedi, M. Erol-Kantarci, and M. Radenkovic, "Integrating renewable energy resources into the smart grid: Recent developments in information and communication technologies," *IEEE Trans. Ind. Inform.*, vol. 14, no. 7, pp. 2814–2825, Jul. 2018.

[2] G. K. Suman, J. M. Guerrero, and O. P. Roy, "Robust frequency control in interconnected microgrids: An H_2/H_∞ control approach," *IEEE Syst. J.*, vol. 16, no. 2, pp. 2044–2055, Jun. 2022.

[3] S. A. Hosseini, M. Fotuhi-Firuzabad, P. Dehghanian, and M. Lehtonen, "Coordinating demand response and wind turbine controls for alleviating the first and second frequency dips in wind-integrated power grids," *IEEE Trans. Ind. Inform.*, vol. 20, no. 2, pp. 2223–2233, Feb. 2024.

[4] A. Ameli, A. Hooshyar, E. F. El-Saadany, and A. M. Youssef, "Attack detection and identification for automatic generation control systems," *IEEE Trans. Power Syst.*, vol. 33, no. 5, pp. 4760–4774, Sep. 2018.

[5] S. M. S. Hussain, A. Latif, M. A. Aftab, C. Konstantinou, A. Al-Durra, and M. A. Abido, "Standardized communication-based diverse structure model predictive controller with demand response for frequency regulation in microgrids," *IEEE Trans. Ind. Appl.*, vol. 60, no. 2, pp. 3554–3567, Mar./Apr. 2024.

[6] K. Singh, M. Amir, F. Ahmad, and M. A. Khan, "An integral tilt derivative control strategy for frequency control in multimicrogrid system," *IEEE Syst. J.*, vol. 15, no. 1, pp. 1477–1488, Mar. 2021.

[7] M. Kumar and Y. V. Hote, "Robust PIDD2 controller design for perturbed load frequency control of an interconnected time-delayed power systems," *IEEE Trans. Control Syst. Technol.*, vol. 29, no. 6, pp. 2662–2669, Nov. 2021.

[8] F. Yang et al., "Fractional-order sliding mode load frequency control and stability analysis for interconnected power systems with time-varying delay," *IEEE Trans. Power Syst.*, vol. 39, no. 1, pp. 1006–1018, Jan. 2024.

[9] A. Oshnoei, M. Kheradmandi, R. Khezri, and A. Mahmoudi, "Robust model predictive control of gate-controlled series capacitor for LFC of power systems," *IEEE Trans. Ind. Inform.*, vol. 17, no. 7, pp. 4766–4776, Jul. 2021.

[10] X.-C. Shangguan, Y. He, C.-K. Zhang, L. Jiang, and M. Wu, "Adjustable event-triggered load frequency control of power systems using control-performance-standard-based fuzzy logic," *IEEE Trans. Fuzzy Syst.*, vol. 30, no. 8, pp. 3297–3311, Aug. 2022.

[11] B. Long, Y. Liao, K. T. Chong, J. Rodríguez, and J. M. Guerrero, "Enhancement of frequency regulation in ac microgrid: A fuzzy-MPC controlled virtual synchronous generator," *IEEE Trans. Smart Grid*, vol. 12, no. 4, pp. 3138–3149, Jul. 2021.

[12] M. V. Kazemi, S. J. Sadati, and S. A. Gholamian, "Adaptive frequency control of microgrid based on fractional order control and a data-driven control with stability analysis," *IEEE Trans. Smart Grid*, vol. 13, no. 1, pp. 381–392, Jan. 2022.

[13] A. Daraz et al., "Load frequency stabilization of distinct hybrid conventional and renewable power systems incorporated with electrical vehicles and capacitive energy storage," *Sci. Rep.*, vol. 14, 2024, Art. no. 9400.

[14] H. R. Baghaee, M. Mirsalim, and G. B. Gharehpetian, "Performance improvement of multi-der microgrid for small-and large-signal disturbances and nonlinear loads: Novel complementary control loop and fuzzy controller in a hierarchical droop-based control scheme," *IEEE Syst. J.*, vol. 12, no. 1, pp. 444–451, Mar. 2018.

[15] M. A. Soliman, H. M. Hasanien, M. S. E. Moursi, and A. Al-Durra, "Chaotic-billiards optimization algorithm-based optimal FLC approach for stability enhancement of grid-tied wind power plants," *IEEE Trans. Power Syst.*, vol. 37, no. 5, pp. 3614–3629, Sep. 2022.

[16] A. Sari, S. Sonmez, S. Ayasun, and Y. Kabalci, "Delay-dependent stability analysis of multi-area LFC-EVS system," *IEEE Trans. Smart Grid*, vol. 14, no. 3, pp. 2178–2188, May 2023.

[17] M. H. Khooban, "An optimal non-integer model predictive virtual inertia control in inverter-based modern ac power grids-based V2G technology," *IEEE Trans. Energy Convers.*, vol. 36, no. 2, pp. 1336–1346, Jun. 2021.

[18] N. Kumari, P. Aryan, G. L. Raja, and Y. Arya, "Dual degree branched type-2 fuzzy controller optimized with a hybrid algorithm for frequency regulation in a triple-area power system integrated with renewable sources," *Protection Control Modern Power Syst.*, vol. 8, no. 3, pp. 1–29, 2023.

[19] M.-H. Khooban, T. Dragicevic, F. Blaabjerg, and M. Delimar, "Shipboard microgrids: A novel approach to load frequency control," *IEEE Trans. Sustain. Energy*, vol. 9, no. 2, pp. 843–852, Apr. 2018.

[20] Z. Pan, F. Dong, J. Zhao, L. Wang, H. Wang, and Y. Feng, "Combined resonant controller and two-degree-of-freedom PID controller for PMSLM current harmonics suppression," *IEEE Trans. Ind. Electron.*, vol. 65, no. 9, pp. 7558–7568, Sep. 2018.

[21] P.-H. Huang, M. S. El Moursi, W. Xiao, and J. L. Kirtley, "Subsynchronous resonance mitigation for series-compensated DFIG-based wind farm by using two-degree-of-freedom control strategy," *IEEE Trans. Power Syst.*, vol. 30, no. 3, pp. 1442–1454, May 2015.

[22] I. Eke et al., "Heuristic optimization based dynamic weighted state feedback approach for 2DOF PI-controller in automatic voltage regulator," *Eng. Sci. Technol., Int. J.*, vol. 24, no. 4, pp. 899–910, 2021.

[23] H. Bevrani, F. Habibi, P. Babahajyani, M. Watanabe, and Y. Mitani, "Intelligent frequency control in an AC microgrid: Online PSO-based fuzzy tuning approach," *IEEE Trans. Smart Grid*, vol. 3, no. 4, pp. 1935–1944, Dec. 2012.

[24] A. Saxena, R. Shankar, S. K. Parida, and R. Kumar, "Demand response based optimally enhanced linear active disturbance rejection controller for frequency regulation in smart grid environment," *IEEE Trans. Ind. Appl.*, vol. 58, no. 4, pp. 4337–4349, Jul./Aug. 2022.

[25] M. Kumar, "Resilient PIDA control design based frequency regulation of interconnected time-delayed microgrid under cyber-attacks," *IEEE Trans. Ind. Appl.*, vol. 59, no. 1, pp. 492–502, Jan./Feb. 2023.

[26] Y. Ho and D. Pepyne, "Simple explanation of the no-free-lunch theorem and its implications," *J. Optim. Theory Appl.*, vol. 115, pp. 549–570, 2002.

[27] A. E. Ezugwu, J. O. Agushaka, L. Abualigah, S. Mirjalili, and A. H. Gandomi, "Prairie dog optimization algorithm," *Neural Comput. Appl.*, vol. 34, no. 22, pp. 20 017–20 065, Jul. 2022.

[28] S. Mahdavi, S. Rahnamayan, and K. Deb, "Opposition based learning: A literature review," *Swarm Evol. Computation*, vol. 39, pp. 1–23, 2018.

[29] C. D. K. Ramos, "Model and control of solar tower for energy production," Ph.D. dissertation, Instituto Superior Tecnico, Lisbon, Portugal, 2015.

[30] A. Latif, S. M. S. Hussain, A. Iqbal, D. C. Das, T. S. Ustun, and A. Al-Durra, "Concurrent frequency–voltage stabilization for hybrid microgrid with virtual inertia support," *IET Renewable Power Gener.*, vol. 17, pp. 2257–2275, 2023, doi: 10.1049/rpg2.12729.

[31] S. Chaine and M. Tripathy, "Performance of CSA optimized controllers of DFIGs and AGC to improve frequency regulation of a wind integrated hydrothermal power system," *Alex Eng. J.*, vol. 58, no. 2, pp. 579–590, 2019.

[32] S. Bhuyan, N. Halder, S. Dey, and S. Paul, "Modified delay compensation in demand response for frequency regulation of interconnected power systems integrated with renewable energy sources," *Cogent Eng.*, vol. 9, no. 1, 2022, Art. no. 2065899.

[33] "NASA surface meteorology and solar energy - available tables," Accessed: Jul. 27, 2023. [Online]. Available: https://eosweb.larc.nasa.gov/cgi-bin/sse/grid.cgi?&num=266111&lat=20.296&hgt=100&submit=Submit&veg=17&sitelev=&email=skip@larc.nasa.gov&p=grid_id&step=2&lon=85.825

[34] S. Debbarma and A. Dutta, "Utilizing electric vehicles for LFC in restructured power systems using fractional order controller," *IEEE Trans. Smart Grid*, vol. 8, no. 6, pp. 2554–2564, Nov. 2017.

[35] S. Izadkhast, P. Garcia-Gonzalez, and P. Frías, "An aggregate model of plug-in electric vehicles for primary frequency control," *IEEE Trans. Power Syst.*, vol. 30, no. 3, pp. 1475–1482, May 2015.

[36] S. A. Pourmousavi and M. H. Nehrir, "Introducing dynamic demand response in the LFC model," *IEEE Trans. Power Syst.*, vol. 29, no. 4, pp. 1562–1572, Jul. 2014.

[37] B. Yildirim, M. Gheisarnejad, and M. H. Khooban, "A new parameter tuning technique for noninteger controllers in low-inertia modern power grids," *IEEE J. Emerg. Sel. Topics Ind. Electron.*, vol. 3, no. 2, pp. 279–288, Apr. 2021.
[38] P. Chen and Y. Luo, "Analytical fractional-order PID controller design with Bode's ideal cutoff filter for PMSM speed servo system," *IEEE Trans. Ind. Electron.*, vol. 70, no. 2, pp. 1783–1793, Feb. 2023.
[39] K. Singh, M. Amir, F. Ahmad, and S. S. Refaat, "Enhancement of frequency control for standalone multi-microgrids," *IEEE Access*, vol. 9, pp. 79128–79142, 2021.
[40] "IEEE PES load data," Accessed: Jan. 19, 2021. [Online]. Available: http://site.ieee.org/pes-iss/data-sets/
[41] P. Babahajiani, Q. Shafee, and H. Bevrani, "Intelligent demand response contribution in frequency control of multi-area power systems," *IEEE Trans. Smart Grid*, vol. 9, no. 2, pp. 1282–1291, Mar. 2018.

ABDUL LATIF (Member, IEEE) received the B.Tech. degree in electrical engineering from Aliah University, Kolkata, India, in 2014, the M.Tech. degree in electrical engineering from the National Institute of Technology Agartala, Agartala, India, in 2016, and the Ph.D. degree from the Department of Electrical Engineering, National Institute of Technology Silchar, Silchar, India, in 2021, with a Scholarship from the Ministry of Human Resources Development (M.H.R.D), Government of India.

During the Ph.D. degree, he was the recipient of the DAAD Fellowship to attend an internship with Technical University, Dresden, Germany. In addition, he has completed a six-month project with Fukushima Renewable Energy Institute, AIST, Koriyama, Japan. Later, he worked as a Research Associate with ESCO Lab, Advanced Power and Energy Center, EECS Department, Khalifa University, Abu Dhabi, UAE. He is currently working as a Postdoctoral Researcher with Nantes University, Nantes, France. His research interests include microgrid operation and control, power system stability, mobile microgrid, soft computing techniques, artificial intelligent control design, and smart grids.

Dr. Latif was the recipient of the Award for Outstanding Reviewer for IEEE TRANSACTIONS ON SUSTAINABLE ENERGY in 2022, and also the Best Doctoral award of the Institute from the National Institute of Technology Silchar. He is also on the Editorial Board (Review Editor for Smart Grid) for *Frontiers in Energy*.

S. M. SUHAIL HUSSAIN (Senior Member, IEEE) received the Ph.D. degree in electrical engineering from Jamia Millia Islamia (a Central University), New Delhi, India, in 2018.

He is currently an Assistant Professor with the Electrical Engineering Department, King Fahd University of Petroleum and Minerals (KFUPM), Dhahran, Saudi Arabia. He is also an Affiliate with the Interdisciplinary Research Center for Renewable Energy and Power Systems and a Fellow with K.A.CARE Energy Research and Innovation Center, KFUPM. Prior to that, he was an AIST Postdoctoral Researcher with Fukushima Renewable Energy Institute, AIST (FREA), Koriyama, Japan, and a Senior Research Fellow with the Department of Computer Science, National University of Singapore, Singapore. His research interests include power system communication, cybersecurity in power systems, and substation automation.

Dr. Hussain was the recipient of the IEEE Standards Education Grant approved by the IEEE Standards Education Committee for implementing project and submitting a student application paper in 2014–2015. He is an Associate Editor for the IEEE OPEN JOURNAL OF POWER AND ENERGY.

AHMED AL-DURRA (Senior Member, IEEE) received the B.Sc., M.Sc., and Ph.D. degrees in electrical and computer engineering from The Ohio State University, Columbus, OH, USA, in 2005, 2007, and 2010, respectively.

He is currently a Professor with the Electrical Engineering and Computer Science Department, Khalifa University, Abu Dhabi, UAE, where he is also an Associate Provost for Research. He has supervised or cosupervised more than 30 Ph.D./master's students. He is leading the Energy Systems Control and Optimization Laboratory under the Advanced Power and Energy Center. He has more than 260 scientific papers in top-tier journals and refereed international conference proceedings. His research interests include applications of control and estimation theory on power systems stability, micro and smart grids, renewable energy systems and integration, and process control.

Dr. Al-Durra is the Editor for IEEE TRANSACTIONS ON SUSTAINABLE ENERGY and IEEE POWER ENGINEERING LETTERS, and an Associate Editor for the IEEE TRANSACTIONS ON INDUSTRY APPLICATIONS, *IET Renewable Power Generation*, and *Frontiers in Energy Research*.

ATIF IQBAL (Fellow, IEEE) received the B.Sc. (Gold Medal) and M.Sc. (power system and drives) degrees in engineering from the Aligarh Muslim University (AMU), Aligarh, India, in 1991 and 1996, respectively, and the Ph.D. degree in electrical engineering from Liverpool John Moores University, Liverpool, U.K., in 2006.

He is currently a Professor of electrical engineering with Qatar University, Doha, Qatar. He is also a former Full Professor of electrical engineering with AMU. Since 1991, he has been employed as a Lecturer with the Department of Electrical Engineering, AMU, where he served as a Full Professor, until August 2016. He has published widely his research findings related to power electronics and renewable energy sources in international journals and conferences. He has authored or coauthored more than 300 research articles, one book, and three chapters in two other books. His research interests include modeling and simulation of power electronic converters, control of multiphase motor drives and renewable energy sources, solar photovoltaic systems, and metaheuristic algorithms.

Dr. Iqbal was the recipient of the Outstanding Faculty Merit Award AY and the Research Excellence Award at Qatar University, Doha, Qatar, from 2014 to 2015, and the Maulana Tufail Ahmad Gold Medal for standing first at the B.Sc. engineering exams with AMU. He has received best research articles including the IEEE ICIT 2013, IET-SEISCON 2013, and SIGMA 2018. He is a Fellow of the IET, U.K., and IE, India. He has supervised several large research and development projects. He is an Associate Editor for the IEEE TRANSACTIONS ON INDUSTRIAL ELECTRONICS and the Editor-in-Chief for the *Journal of Electrical Engineering* (i'manager).